Experimental constraints on shallow differentiation of high-Mg andesite at Whakaari, New Zealand

Wei-Cheng Jiang, John Adam, Chris Firth, Caroline Martel, Simon Turner, Tracy Rushmer, Shane Cronin

Contributions to Mineralogy and Petrology (2025) 180:48
https://doi.org/10.1007/s00410-025-02235-3

ORIGINAL PAPER

Experimental constraints on shallow differentiation of high-Mg andesite at Whakaari, New Zealand

Wei-Cheng Jiang[1] · John Adam[1] · Chris Firth[1,2] · Caroline Martel[3] · Simon Turner[1] · Tracy Rushmer[1] · Shane Cronin[4]

Received: 3 September 2024 / Accepted: 18 June 2025

Abstract

Phase equilibrium experiments were used to determine conditions of melt evolution and phenocryst growth in high-Mg andesite magmas that were erupted at Whakaari (White Island) in New Zealand between 1976 and 2000. The high-Mg andesites are both mafic (7.21–10.3 wt% MgO) and silica-rich (55.3–58.6 wt% SiO_2) with phenocrysts of plagioclase, orthopyroxene, clinopyroxene, olivine, Cr-spinel and Fe–Ti oxides contained in a glassy to fine-grained matrix of mostly dacitic composition. Experiments were conducted on one of the most primitive samples available (the high-Mg andesite TRW34) at conditions ranged from 1 atm to 500 MPa at temperatures of 950 to 1200 °C with total water concentrations of 0 to 10 wt%. Except for the 500 MPa experiments, fO_2 was buffered at 1 or 2 log units above Ni–NiO. Consistent with earlier thermodynamic modelling, our results demonstrate that residual Whakaari melts (now represented by matrix glasses) evolved along a plagioclase + two-pyroxene cotectic (± magnetite ± ilmenite) under comparatively low-pressure, shallow conditions (< 200 MPa or < 6 km) and were relatively hot (> 950 °C) and dry (≤ 3 wt% melt-H_2O), with oxygen fugacities either at, or slightly above Ni–NiO + 1 log unit. Although the bulk-rock trends of Whakaari volcanic rocks are clearly calc-alkaline, those of the residual matrix glasses are only weakly so. A likely explanation for this contrast is that the primary magmas were relatively hydrous, but became dehydrated when intruded at shallow depths. The effectiveness of water in this role, combined with the demonstrable presence of primitive calc-alkaline magmas in the upper-crust, highlights the importance of magmatic water, in place of deep crustal fractionation, for shaping the calc-alkaline evolutionary trend.

Keywords Whakaari · Arc volcano · Experimental petrology · Shallow magma differentiation · High-Mg andesite

Introduction

Conditions of pre-eruptive magma storage (e.g., pressure, temperature, fO_2, and volatile activity) play a significant role in controlling the degree of hazard posed by volcanic eruptions (Cashman and Giordano 2014; Cashman and Sparks 2013; Popa et al. 2021; Scaillet et al. 2008). They also have a bearing on historical debates concerning the origin of the calc-alkaline magma series in arc settings [e.g., (Chin et al. 2018; Grove et al. 2003; Sisson and Grove 1993; Zimmer et al. 2010)]. Historically, a variety of approaches have been used to constrain the conditions of magma storage prior to eruptions. These include mineral thermobarometers (Neave and Putirka 2017; Phillips and Till 2021), thermodynamic models (Almeev et al. 2013; Cashman and Edmonds 2019; Cordell et al. 2022; Ghiorso and Gualda 2015; Gualda et al. 2012), geophysical surveys (Elsworth et al. 2008; Magee et al. 2018; Peltier et al. 2009), and

Communicated by Othmar Müntener.

✉ Wei-Cheng Jiang
jiangwc5110@gmail.com

[1] School of Natural Sciences, Macquarie University, Wallumattagal Campus, 12 Wally's Walk, Macquarie Park, Sydney, New South Wales 2109, Australia

[2] School of Earth and Atmospheric Science, Queensland University of Technology, Brisbane, Queensland 4000, Australia

[3] Institut des Sciences de la Terre, Orléans Cedex 2 45071, France

[4] School of Environment, University of Auckland, Auckland 1142, New Zealand

Published online: 17 July 2025

phase-equilibria experiments (Adam et al. 2014; Andújar et al. 2017; Erdmann et al. 2016; Hammer et al. 2002; Melekhova et al. 2015, 2017).

Many of these approaches have already been applied at Whakaari (also known as White Island), an andesite-dacite stratovolcano offshore from New Zealand's North Island. This volcanic island is currently active and exhibits frequent signs of unrest (Cole et al. 2000; Kilgour et al. 2021a) including an incident during 2019 when a small but unexpected eruption killed 22 people (Dempsey et al. 2020). A preceding series of larger Strombolian eruptions occurred between 1976 and 2000 and produced unusual high-Mg andesite magmas (Mg# > 70, SiO_2 > 55 wt%, where Mg# = 100 × molar MgO/(FeO + MgO). It is the conditions of pre-eruptive storage for these magmas that are the focus of this study.

Previous research has already suggested a diverse range of conditions that are consistent with either a very shallow reservoir (< 1 km) (Esposito et al. 2014; Mandon et al. 2021; Rapien et al. 2003; Wardell et al. 2001) and/or a deeper mid-crustal (7–9 km?) reservoir (Cole et al. 2000; Kilgour et al. 2021b). Such variation favours the idea of a "trans-crustal plumbing system", such as is now popularly applied to arc volcanoes (Cashman et al. 2017; Giordano and Caricchi 2022; Journeau et al. 2022). However, there are potential problems with the evidence for Whakaari. For example, volatile concentrations (which are critical to modelling) have been determined from melt inclusions but may be affected by degassing (Collins et al. 2009; Esposito et al. 2014). The accuracy of the mineral-melt based thermobarometers previously applied to arc volcanoes (e.g., (Jorgenson et al. 2022; Petrelli et al. 2020; Putirka 2008) have also been questioned (Wieser et al. 2023a, b). Some modelling results also suggested that the magma evolved both with very low water concentrations (1 wt%) and at low pressure (100 MPa) (Severs et al. 2009), while others have proposed water-saturated conditions at higher pressures (150 MPa) (Hughes et al. 2024). In addition, numerous geophysical techniques (e.g., seismology, ground deformation and magnetotellurics) have so far failed to reveal the deep magmatic system that has been postulated to exist beneath Whakaari (Clark and Otway 1989; Nishi et al. 1996; Peltier et al. 2009).

To better understand these issues we conducted an experimental investigation of one of the most primitive 1976–2000 high-Mg andesites (sample TRW34). This was used to examine the effects of pressure, temperature, fO_2, and melt-water concentrations on liquidus relationships. The results are compared with relationships for co-existing phenocrysts and matrix glasses (melts) in the natural rocks to constrain conditions of pre-eruptive storage and evolution for the high-Mg andesite magmas. Our conclusions are compared with the results of earlier thermodynamic modelling by (Jiang et al. 2024).

Volcanic geology of Whakaari

Whakaari lies at the northern-most end of the Taupo Volcanic Zone (TVZ) a region of frequent tectonic and magmatic activity during the last ~ 2 Ma (Cole et al. 2000; Spinks et al. 2005; Wilson and Rowland 2016). The volcano forms an island ~ 50 km offshore in the Bay of Plenty (Kilgour et al. 2021a). Although its exposed lavas are mostly high-silica andesites and dacites, they include a suite of high-Mg andesites that were erupted in 1976–2000 (Cole et al. 2000).

All of the volcanic rocks are calc-alkaline and display typical arc-related geochemical signatures (Clark and Cole 1986; Cole et al. 2000). The rocks are porphyritic with phenocrysts of plagioclase, clinopyroxene, and orthopyroxene, combined with rare olivine and a few Cr-spinel and Fe–Ti oxides (Cole et al. 2000). Matrices are glassy to wholly crystalline and mostly of dacitic composition. Melt inclusions are abundant in all of the silicate phenocryst phases and can be divided into two separate groups. The first occurs only in olivine whereas the second is equally characteristic of plagioclase, clinopyroxene and orthopyroxene. There is complete overlap in the compositions of melt inclusions in plagioclase, clinopyroxene and orthopyroxene. This is replicated in the compositional range of the matrix glasses. The latter define an evolutionary trend from high-Mg andesite to near rhyolite, although most are of broadly dacitic composition. Both the melt inclusions and matrix glasses are depleted in volatiles, with average H_2O, S and Cl concentrations of 0.3 ± 0.2 wt%, 208 ± 268 ppm and 1051 ± 446 ppm, respectively (Kilgour et al. 2021b; Rapien et al. 2003; Wardell et al. 2001).

Experimental investigation of the high-Mg andesite

Experimental strategy

Previously described relationships for matrix glasses and melt-inclusions indicate that residual melts in the high-Mg andesites evolved on a plagioclase plus two-pyroxene cotectic, without olivine being present (Jiang et al. 2024; Rapien et al. 2003). The latter was an earlier crystallising phase that was introduced by mixing with a less crystallised (i.e. near-liquidus) version of the same magma. The removal of olivine during progressive crystallisation can be attributed to the peritectic reaction:

$$\text{Olivine} + \text{melt} \rightarrow \text{orthopyroxene} \quad (1)$$

.

This combination of cotectic and peritectic relationships, and mixing between different states of the same magma forms the basis of our experimental approach. We used two varieties of the starting material. The first was a glass powder prepared from a fused sample of TRW34, and the second a powdered sample of TRW34 that was unfused. Thus, the second contained fragments of the original minerals present in TRW34. The intention was to use the first starting material to investigate equilibrium crystal fractionation, and the second to investigate crystal fractionation where equilibrium is incomplete and occurs in the presence of relict crystals produced by different degrees of fractionation. This second situation is closest to that of the natural magma. This same strategy was used by Erdmann et al. (2016) to study pre-eruptive conditions in complex magmas erupted by Mount Merapi in Indonesia.

The total range of conditions investigated was 1 atm to 500 MPa at temperatures of 950 to 1200 °C, with total water concentrations of 0 to10 wt%, and (except for the 500 MPa experiments) fO_2 at 1 or 2 log units above Ni–NiO. Three different apparatus were used for experiments. These included:

1. An end-loaded piston-cylinder apparatus for experiments at 500 MPa.
2. Internally-heated pressure vessels at 200 MPa.
3. Vertical muffle-tube furnaces at 1 atm.

The 500 MPa experiments were intended to represent lower-crustal conditions (equivalent to 18–19 km) as suggested by recent seismic data (Gase et al. 2019). Mid-crustal differentiation is simulated by the 200 MPa runs, while 1 atm runs were used to explore near-surface differentiation.

Starting materials

The starting material used in all runs was based on the high-Mg andesite TRW34 (Table 1) that was erupted at Whakaari in 1977. This contains phenocrysts of plagioclase (20–25%), clinopyroxene (8–10%), orthopyroxene (< 10%), olivine (< 5%) magnetite (< 1%), and Cr-spinel (< 1%) in a glassy to partially-crystalline matrix of dacitic composition. For experiments using glass as the starting material the glass was prepared by fusing a 1 g sample of the powdered natural rock in a 1 atm furnace for 30 min at 1250 °C (beyond dry liquidus) and then quenching in water. The composition of the resulting glass was checked by electron microprobe (see section below) and the glass then crushed and ground in an agate mortar before being used in the experimental

Table 1 Starting compositions of all experiments (wt%)[a]

Sample	SiO_2	TiO_2	Al_2O_3	Cr_2O_3	FeO^T	CaO	MgO	MnO	NiO	K_2O	Na_2O	P_2O_5
TRW34	58.13	0.66	13.74	0.06	7.01	8.19	8.22	0.14	0.01	1.43	2.44	0.08

a. All the values have been normalised to 100%

runs. For experiments on natural rock powders a sample of TRW34 that had previously been crushed in a Tema® mill was re-ground in an agate mortar and pestle to a grain size of 10–50 µm before being dried and used in the experiments.

Piston-cylinder experiments

Experiments at 500 MPa were performed at Macquarie University using end-loaded piston-cylinder apparatus of the type described by Boyd and England (1960). Temperatures varied from 950 to 1200 °C with either 2 or 10 wt% of added water (the latter concentration being sufficient to induce water-saturation at 0.5 GPa). Furnace assemblies were of 12.7 mm in diameter and 32 mm in length. For experiments with 10 wt% H_2O talc sleeves were used, whereas for experiments with 2 wt% H_2O an inner sleeve of boron nitride in combination with a talc outer sleeve was used. This guarded against the possibility of unwanted water addition by the dehydration of the talc outer sleeves. Heat was provided by cylindrical graphite resistance heaters. Internal components were made of ALSIMAG (a porous ceramic composed of MgO, Al_2O_3 and SiO_2).

Sample capsules were made of $Ag_{70}Pd_{30}$ tubing with an inner diameter of 1.8 mm and an outer diameter of 2.2 mm. Capsules were sealed using a PUK 3 spot-welder. Before loading, powdered starting materials were dried at 110 °C. Deionized water was first added to capsules using a graduated micro syringe. The powdered starting materials was added subsequently. The total sample mass for each experiment was 15 mg. During welding, loaded capsules were wrapped in wet tissue to prevent heating and water loss. At all stages of capsule preparation a careful check of weights was maintained to guard against the loss of starting materials. Finally, the integrity of the capsules was checked by placing sealed capsules in an oven at 110 °C for ten minutes. Weights were then re-checked to test for possible water loss.

Temperature was regulated using S-type thermocouples paired with Eurotherm® controllers and no corrections were made to account for pressure-induced effects on electromagnetic force. Pressure was manually applied via a hydraulic pump using a cold piston-in technique. A—10% adjustment to measured pressures was made to allow for the effects of friction on the furnace type used (Green et al. 1966). Depending on temperatures, run times varied from 24 to 62 h. Although oxygen fugacity was unbuffered it is believed to have been between the Ni–NiO and magnetite-wustite (MW) buffers (Green 1976). At the conclusion of the experiments, runs were quenched by switching off the power supply to the furnaces. This produced quench rates of > 100 °C/second.

Internally heated pressure vessel experiments

The 200 MPa experiments were conducted at the Institut des Sciences de la Terre d Orléans, France using vertical, internally-heated pressure vessels (IHPV) that employed mixed H_2–Ar gas as the pressurising medium. This allowed oxygen fugacities to be buffered by controlling the proportions of Ar and H_2 in the pressure medium. Temperatures were controlled and monitored using two S-type thermocouples and a Eurotherm 906 EPC controller and are believed accurate to within ± 5 °C. A pressure transducer was used to simultaneously monitor pressure with an accuracy of ± 2 MPa. Near isothermal conditions (with a thermal gradient of 2–3 °C) for a 3 cm long hotspot were achieved using a double-winding high-temperature molybdenum furnace. $Au_{80}Pd_{20}$ capsules were employed for all runs. These had inner and outer diameters of 2.5 mm and 2.9 mm, respectively. Each capsule contained 30 mg of powdered sample material along with variable amounts of water and CO_2 (X_{H2O} = 1, ~ 0.7 and ~ 0.3); water was added using a 10 mL syringe, with CO_2 added as $Ag_2C_2O_4$. The latter was used to regulate the activity of H_2O in coexisting fluids and it is not expected to independently affect phase equilibria. The sample materials were the same as used for the piston-cylinder experiments.

A two-step procedure was employed to confirm the watertight integrity of capsules. The first involved submerging capsules in a hot silicone solution to check for escaping bubbles. Capsules were then placed in an oven for several hours at 120 °C before being re-weighed. Experiments typically ran for 40 to 72 h depending on the temperatures used. The majority of runs were buffered at NNO + 1 while one run was buffered at NNO + 2 (R5). Quenching involved application of a high-power current to fuse the platinum wire on which sample capsules were suspended. This caused the sample-capsules to fall to the cold bottom-section of the ceramic furnace tube. A successful quench could be verified by observing a rise of pressure in the furnace vessel to ~ 3–5 MPa with a quench rate of > 100 °C/second.

One-atmosphere experiments

1 atm experiments were performed at the Research School of Earth Sciences at the Australian National University. Powdered glass starting material was divided into aliquots and combined with polythene oxide reagent to make a paste. This was loaded onto loops of Fe-doped platinum wire (of 0.25 mm diameter) resulting in beads of 3–5 mm diameter after melting in a furnace. The Fe-doped platinum wire was made by immersing Pt-wire loops in the sample powder (contained in a well-used Pt bucket) followed by melting the powder at 1300 °C for 30 min. The adhering glass was then removed using HF. This procedure was effective in

Table 2 Experimental conditions and products

Run No.	T (°C)	Hrs	Run products[a]	Phase proportions (%)[b]	Fe loss (rel. %)[c]	H_2O (wt%)[d]	X H_2O	Melt H_2O (wt%)	logfO_2 ($\triangle$NNO)	Kd (Fe-Mg)$^{2+}$[e]	Kd (Ca-Na)
Fused glass starting material											
500 MPa water-saturated											
RUN2159	1100	32	Gl+Ol+Cpx+Opx	$93.6^{0.1}_{2.3}+1.8^{1.1}_{0.7}+1.6^{0.9}_{0.6}+1.9^{1.1}_{1.7}$	11.89	10.78	1	9.92[f]	<0	Ol: 0.330 **Cpx: 0.322** **Opx: 0.337**	
RUN2149	1050	50	Gl+Ol+Cpx+Opx	$83.7^{0.2}_{2.7}+3.4^{1.8}_{1.2}+8.6^{0.8}_{1.0}+4.3^{2.8}_{1.8}$	6.13	10.22	1	10.1	<0	**Cpx: 0.282** **Opx: 0.292**	
RUN2152	1000	49	Gl+Cpx+Opx	$75.9^{0.6}_{0.4}+12.8^{1}_{0.9}+11.3^{0.7}_{0.7}$	8.9	9.76	1	10.32	<0	**Cpx: 0.276** **Opx: 0.341**	
RUN2153	950	62	Gl+Cpx+Opx+Amp+Mag	$63.8^{1.1}_{3.3}+10.7^{1.9}_{1.9}+6.3^{1.6}_{1.8}+17.6^{4.7}_{5.8}+1.7^{0.2}_{0.3}$		10.32	1	10.68	<0	Cpx: 0.288 Opx: 0.386	
500 MPa Water-undersaturated											
RUN2156	1150	24	Gl+Cpx+Opx	$82.2^{0.7}_{0.8}+7.7^{0.9}_{1.1}+10.1^{0.4}_{0.4}$	13.29	2.35	1	2.84[g]	<0	**Cpx: 0.293** **Opx: 0.302**	
RUN2157	1100	46	Gl+Cpx+Opx+Plag	$59.7^{2.0}_{2.2}+16.2^{0.2}_{0.7}+10.9^{0.5}_{0.6}+13.3^{1.7}_{1.6}$	44.93	1.88	1	2.99 (5.43, 6.75)[h]	<0	Cpx: 0.271 Opx: 0.286	Plag: 1.482
RUN2158	1050	48	Gl+Cpx+Opx+Plag	$48.0^{1.8}_{1.8}+18.0^{0.6}_{0.7}+13.0^{0.5}_{0.6}+20.9^{1.4}_{1.5}$	48.06	2.24	1	4.46 (3.99, 7.53)	<0	Cpx: 0.223 Opx: 0.281	Plag: 2.128
RUN2163	1000	64	Gl+Cpx+Opx+Plag			2.20	1	4.46	<0		
200 MPa water-saturated											
R4A1	1100	40	Gl+Ol+Spl	$95.2^{0.8}_{1.0}+4.7^{0.9}_{1.1}+0.1^{0}_{0}$	10.69	5.78	1	5.60	1	**Ol: 0.337**	
R1A1	1050	48	Gl+Cpx+Opx	$79.6^{0.4}_{0.5}+10.7^{0.6}_{0.6}+9.7^{0.4}_{0.4}$	14.28	5.66	1	5.66	1	**Cpx: 0.345** **Opx: 0.336**	
R3A1	1000	48	Gl+Cpx+Opx+Plag	$59.3^{1.4}_{1.5}+16.2^{0.2}_{0.7}+10.9^{0.5}_{0.6}+10.5^{1.3}_{1.2}$	12.42	5.9	1	5.76 (6.17, 9.68)	1	**Cpx: 0.345** **Opx: 0.336**	Plag: 2.050
R5A1	1000	40	Gl+Cpx+Opx+Plag+Mag	$61.9^{4.1}_{6.4}+18.4^{0.6}_{1.8}+10.8^{3.3}_{4.0}+6.0^{3.8}_{2.5}+2.9^{1.3}_{1.0}$		5.78	1	5.76 (5.61, 9.67)	2	Cpx: 0.338 Opx: 0.251	Plag: 2.395
R2A1	950	72	Gl+Cpx+Opx+Plag+Ilm	$26.0^{4.5}_{4.2}+20.2^{1.6}_{1.2}+21.3^{2.3}_{2.1}+32.3^{3.0}_{2.7}+0.2^{0.1}_{0.1}$		5.77	1	5.85 (4.49,10.28)	1	Cpx: 0.336 Opx: 0.377	Plag: 2.348
200 MPa water-undersaturated											
R4A2	1100	40	Gl+Cpx+Opx	$80.9^{0.3}_{0.4}+9.9^{0.6}_{0.6}+9.2^{0.4}_{0.4}$	23.06	2.8	0.7	4.70[i]	1	**Cpx: 0.296** **Opx: 0.303**	
R4A3	1100	40	Gl+Cpx+Opx+Plag	$50.0^{2.9}_{3.8}+22.4^{2.1}_{2.3}+7.8^{1.9}_{2.3}+19.8^{2.0}_{2.2}$	35.98	0.94	0.31	2.68 (5.48, 6.15)	1	Cpx: 0.317 Opx: 0.276	
R1A2	1050	48	Gl+Cpx+Opx+Plag	$43.8^{1.4}_{1.5}+19.4^{1.0}_{1.0}+12.9^{0.9}_{0.9}+23.8^{1.4}_{1.4}$	23.94	2.83	0.7	4.77 (5.70, 7.47)	1	Cpx: 0.259 Opx: 0.268	Plag: 2.905
R3A2	1000	48	Gl+Cpx+Opx+Plag	$36.9^{2.2}_{2.4}+19.9^{1.7}_{1.7}+13.2^{1.3}_{1.3}+29.9^{1.8}_{1.9}$	24.07	2.49	0.67	4.75 (4.90, 8.42)	1	Cpx: 0.317 Opx: 0.367	Plag: 1.811

Table 2 (continued)

Run No.	T (°C)	Hrs	Run products[a]	Phase proportions (%)[b]	Fe loss (rel. %)[c]	H_2O (wt%)[d]	X H_2O	Melt H_2O (wt%)	logfO_2 ($\triangle$NNO)	Kd $(Fe\text{-}Mg)^{2+e}$	Kd (Ca-Na)
R5A2	1000	40	Gl + Cpx + Opx + Plag + Mag	Mag: 0.6 ± 0.2[j]		1.54	0.33	3.36	2		
R2A2	950	72	Gl + Cpx + Opx + Plag + Ilm			2.79	0.7	4.91	1		
1 atm anhydrous											
R1220GL	1220	4	Gl + Opx	$98.8^{0.2}_{0.3}+1.2^{0.3}_{0.2}$	1.73	0	0	0	1	**Opx: 0.311**	
R1180GL	1180	6	Gl + Opx	$91.7^{1.1}_{1.2}+8.3^{1.2}_{1.1}$	6.62	0	0	0	1	**Opx: 0.262**	
R1150GL	1150	15	Gl + Opx	$92.6^{0.3}_{0.3}+7.4^{0.3}_{0.3}$	2.15	0	0	0	1	**Opx: 0.257**	
R1120GL	1120	24	Gl + Cpx + Opx + Plag + Mag	$46.8^{3.9}_{4.2}+10.6^{3.5}_{3.5}+18.0^{5.5}_{5.8}+22.9^{3.2}_{4.5}+1.8^{0.4}_{0.5}$		0	0	0	1	**Cpx: 0.307** **Opx: 0.225**	Plag: 1.575
Unfused whole rock starting material											
500 MPa water-saturated											
RUN2128	1100	48	Glass + Ol + Cpx + Spl	$93.7^{0.4}_{0.8}+5.8^{0.3}_{0.4}+0.4^{0.5}_{0.2}+0.1^{0}_{0}$	9.93	10.45	1	9.93	< 0	**Cpx: 0.281**	
RUN2127	1050	49	Glass + Cpx + Opx	$76.8^{0.6}_{0.7}+12.8^{0.7}_{0.7}+10.4^{0.4}_{0.4}$	19.13	9.76	1	10.15	< 0	**Cpx: 0.306** **Opx: 0.317**	
RUN2129	1000	48	Glass + Cpx + Opx + Plag	$47.2^{1.7}_{1.8}+15.6^{0.5}_{0.6}+15.0^{0.4}_{0.4}+22.1^{1.6}_{1.7}$	9.26	9.54	1	10.52	< 0	**Cpx: 0.278** **Opx: 0.247**	Plag: 2.501
500 MPa Water-undersaturated											
RUN2138	1150	24	Glass + Cpx + Opx	$85.4^{0.4}_{0.5}+4.3^{0.6}_{0.7}+10.2^{0.4}_{0.4}$	16.55	2.31	1	2.69	< 0	Cpx: 0.312 Opx: 0.319	
RUN2137	1100	46	Glass + Cpx + Opx	$77.8^{0.4}_{0.5}+11.8^{0.6}_{0.6}+10.3^{0.4}_{0.4}$	14.54	1.86	1	2.35	< 0	**Cpx: 0.297** **Opx: 0.325**	
RUN2165	1050	48	Glass + Cpx + Opx + Plag	$38.5^{1.4}_{1.5}+20.5^{1.0}_{1.1}+13.8^{0.6}_{0.6}+27.7^{1.1}_{1.1}$	48.35	2.25	1	4.52	< 0	**Cpx: 0.310** **Opx: 0.326**	Plag: 4.375
200 MPa water-saturated											
R4A4	1100	40	Glass + Ol + Spl	$96.2^{0.4}_{0.5}+3.7^{0.4}_{0.5}+0.1^{0}_{0}$	3.51	5.45	1	5.57	1	**Ol: 0.349**	
R1A4	1050	48	Glass + Ol + Cpx	$85.7^{0.5}_{0.6}+8.6^{0.7}_{0.7}+5.7^{0.2}_{0.2}$	7.90	5.92	1	5.65	1	**Ol: 0.316** **Cpx: 0.280**	
R3A4	1000	48	Glass + Cpx + Opx	$75.7^{0.4}_{0.4}+14.1^{0.5}_{0.5}+10.2^{0.4}_{0.4}$	11.51	5.5	1	5.68	1	**Cpx: 0.319** **Opx: 0.276**	
R5A3	1000	40	Glass + Cpx + Opx + Mag	$74.7^{0.5}_{0.5}+13.9^{0.6}_{0.5}+8.3^{0.3}_{0.3}+3.2^{0.1}_{0.1}$		5.96	1	5.8	2	Cpx: 0.285 Opx: 0.254	
R2A4	950	72	Glass + Cpx + Opx + Plag + Mag	$44.9^{3.1}_{2.3}+18.1^{2.5}_{3.2}+19.0^{3.0}_{2.3}+16.7^{3.2}_{3.4}+1.2^{0.3}_{0.3}$		6.08	1	5.82	1	**Cpx: 0.297** **Opx: 0.309**	Plag: 6.22
200 MPa water-undersaturated											
R4A5	1100	40	Glass + Cpx + Opx	$84.3^{0.3}_{0.4}+5.7^{0.5}_{0.5}+10.0^{0.3}_{0.3}$	17.50	2.84	0.7	4.69	1	**Cpx: 0.291** **Opx: 0.317**	

Table 2 (continued)

Run No.	T (°C)	Hrs	Run products[a]	Phase proportions (%)[b]	Fe loss (rel. %)[c]	H_2O (wt%)[d]	X H_2O	Melt H_2O (wt%)	logfO_2 ($\triangle$NNO)	Kd (Fe-Mg)$^{2+}$[e]	Kd (Ca-Na)
R1A5	1050	48	Glass+Cpx+Opx	$75.0^{0.3}_{0.3}$+$13.9^{0.5}_{0.5}$+$11.1^{0.3}_{0.3}$	16.74	2.93	0.69	4.74	1	**Cpx: 0.317** **Opx: 0.305**	
R3A5	1000	48	Glass+Cpx+Opx+Plag	$50.9^{1.1}_{1.2}$+$15.4^{0.5}_{0.5}$+$16.0^{0.5}_{0.5}$+$17.7^{0.9}_{1.0}$	9.82	2.69	0.67	4.68	1	**Cpx: 0.282** **Opx: 0.264**	Plag: 2.85
R2A5	950	72	Glass+Cpx+Opx+Plag+Ilm	$38.1^{2.1}_{1.3}$+$17.0^{1.5}_{2.2}$+$18.7^{1.0}_{1.3}$+$25.9^{2.2}_{2.4}$+$0.3^{0.2}_{0.1}$		2.82	0.7	4.88	1	**Cpx: 0.298** **Opx: 0.294**	
1 atm anhydrous											
R1220M	1220	4	Glass+Opx+Plag	$82.4^{2.5}_{3.6}$+$9.3^{1.5}_{1.6}$+$8.4^{2.2}_{1.8}$	3.95	0	0	0	1	**Opx: 0.317**	Plag: 1.131
R1180M	1180	6	Glass+Cpx+Opx+Plag	$81.0^{2.5}_{4.4}$+$3.0^{2.0}_{1.3}$+$11.2^{0.5}_{0.9}$+$4.8^{1.5}_{2.1}$	18.96	0	0	0	1	**Cpx: 0.347** **Opx: 0.324**	Plag: 1.255
R1150M	1150	15	Glass+Opx+Plag	$81.1^{1.9}_{2.2}$+$11.2^{0.5}_{0.5}$+$7.7^{1.8}_{1.4}$	16.70	0	0	0	1	**Opx: 0.250**	Plag: 1.304
R1120M	1120	24	Glass+Cpx+Opx+Plag+Mag	$56.3^{3.5}_{4.3}$+$12.6^{2.5}_{1.9}$+$12.7^{1.8}_{2.3}$+$18.2^{2.7}_{3.5}$+$0.1^{0.1}_{0.1}$		0	0	0	1	**Cpx: 0.321** **Opx: 0.243**	Plag: 2.46

a: Phase abbreviations: Gl=glass; Cpx=clinopyroxene; Opx=orthopyroxene; Ol=olivine; Plag=plagioclase; Amp=amphibole; Spl=Cr-rich Spinel (including chromite and hercynite as per classification in Figure SI 3); Mag=magnetite; Ilm=ilmenite

b: Phase proportions calculated by mass balance without FeO and NiO. $93.6^{0.1}_{2.3}$ is equal to $93.6 \pm \frac{0.1}{2.3}$, where 93.6 represents the best fitting phase abundance calculated by the algorithm from Prissel et al. (2023), 0.1 and 2.3 are the phase abundance increments to the 25th (−) and 75th (+) percentiles of the posterior distribution

c: Apparent loss or gain of FeO estimated as $100*(FeO_{calculated}–FeO_{starting\ material})/FeO_{starting\ material}$

d: Nominated H_2O content in the run, calculated by weight proportions of water mixed with the starting material

e: The bolded Fe-Mg exchange ratios were calculated using ferrous iron (Fe^{2+}) in both glass and minerals. The ferrous iron in glass and mineral was calculated using approach from Kress and Carmichael (1991) and Droop (1987), respectively. The non-bolded ratios were calculated using the total Fe concentrations

f: Calculated by $H_2O–CO_2$ solubility model (Ghiorso and Gualda 2015) using VESICal (Iacovino et al. 2020)

g: Calculated by multiplying the nominal water content by the proportion of glass, assuming all the water is in the glass

h: The two values in the bracket represent results calculated from liquid-plagioclase hygrometry (left– Putirka (2005); right– Waters and Lange (2015)

i: Calculated by an empirical model. Please refer to the main text for details

j: The phase proportion of magnetite was calculated by the proportion of area on the BSE image

preventing iron loss from the samples to the Pt wire during the experiments. All experiments were buffered at around one log unit above Ni–NiO. This was achieved by upward flow of CO and CO_2 gas mixtures regulated by Tylan F2800 mass flow controllers (Firth et al. 2019). The ratio of CO_2 to CO gas varied from 140:1 to 160:1 across temperatures from 1220 to 1120 °C. While avoid the loops touching and adhering either to the muffle tube's sides or to one another, the samples were initially placed in the furnace at ~600 °C. The flow of CO and CO_2 gases was then commenced with a ramp rate of 6 °C/min to the final run temperature. A type B thermocouple ($Pt_{94}Rh_6$–$Pt_{70}Rh_{30}$), positioned outside the muffle tube, was used to monitor temperatures during the experiments while avoiding exposure to the CO-CO_2 gas mixture. A second type B thermocouple was used for temperature measurement inside the muffle tube. The difference between the two thermocouples remained within the range of 10–15 °C, indicating that the thermocouple was not significantly compromised by gas-induced interference. The experiments were run for 4–24 h depending on the temperature. After the completion of experiments, the samples were quenched by dropping them into water.

Analysis

Run products were mounted in epoxy before being polished and analysed using a Zeiss EVO scanning electron microscope (SEM) in the Macquarie University GeoAnalytical facility (MQGA). Backscattered electron (BSE) images were obtained in conjunction with quantitative major element analyses using an Oxford Ultim Max 100 energy dispersive spectrum (EDS) detector. For EDS analysis, C.M. Taylor corporate standards were employed for spectra calibration, with olivine used for Mg, albite for Na, orthoclase for Si, O, and K, spessartine for Mn, kyanite for Al, chromite for Cr, pure Fe_2O_3 for total Fe, diopside for Ca, synthetic TiO_2 for Ti, and synthetic $Eu(PO_3)_3$ for P. A pure Cu standard was used to calibrate the beam current and was regularly tested during analyses. The working distance was kept at 12 mm for both standards and unknowns to maximize the quantitative accuracy of analyses. For silicate and oxide minerals (olivine, plagioclase, pyroxenes, Cr-spinel, magnetite, and ilmenite), a 20 kV voltage and 10 µA beam current were used, together with counting times of 30 s. However, for hydrous SiO_2-rich glasses the counting time limited to ten seconds and analyses performed as scans of delineated areas. This was required to minimize Na loss during analyses. The USGS standard BHVO-2g was regularly analysed to monitor the accuracy of analyses (Fig. SI 1). Analytical results for anhydrous minerals were only considered if EDS totals fell between 98 and 102 wt% and cation totals were close to their ideal values. For some experiments (R5A2, R2A2, and RUN2163) mineral phases were visible under BSE imaging but could not be quantitatively analysed owing to their small size (<5 µm diameter) and interference from nearby phases. However, the analytical results were usually sufficient for the identity of the mineral phase to be determined.

Estimating the water concentrations of melts during experiments

H_2O concentrations in water-saturated melts were calculated using published H_2O–CO_2 solubility models (Ghiorso and Gualda 2015). For water-undersaturated melts, H_2O concentrations were determined by dividing the initial water concentration of the starting material by the mass fraction of melt produced in each experiment. This was possible because melt was the only hydrous phase produced in most experiments (Table 2). Because a mixed H_2O–CO_2 fluid was adopted in the IHPV experiments, a second approach was to derive the fH_2O for each water-undersaturated run following the relationship $fH_2O = f^oH_2O \times XH_2O$, where f^oH_2O (bars) $= aH_2O_{melt}$ (wt %)^b, in which a = 51.19 and b = 2.06 based on the empirical fits of Papale et al. (2006). The method is described in more detail by Andújar et al. (2017).

For experiments where a relatively high Fe-loss (>15%; Table 2) occurred, it is possible that water gain occurred due to the reduction of FeO to Fe and a balancing diffusion of H released by dehydrated talc into the capsules (Kägi et al. 2005). To test for this, plagioclase-melt hygrometers were applied to experiments containing plagioclase (Table 2).

Results

A list of run conditions and products for individual experiments are provided in Table 2 and illustrated in Figs. 1 and 2. Mineral compositions are presented in Table 3 and in Figs. 3, 4 and 5 and SI 2–6. The mineral phases produced in experiments included clinopyroxene, orthopyroxene, olivine, plagioclase, Cr-spinel, magnetite, ilmenite, and amphibole. Glass was produced in all experiments.

Description of run products

Olivine and Cr-spinel were produced in some near-liquidus runs on glass starting material (Figs. 1 and 2a and d) where the olivine occurs as relatively large (25–100 µm) euhedral crystals with Cr-spinel present as small grains (<10 µm) in both the matrix glass and as inclusions in olivine. Clinopyroxene and orthopyroxene are the most common silicate minerals in most subliquidus experiments including those on glass starting materials. In these, orthopyroxene

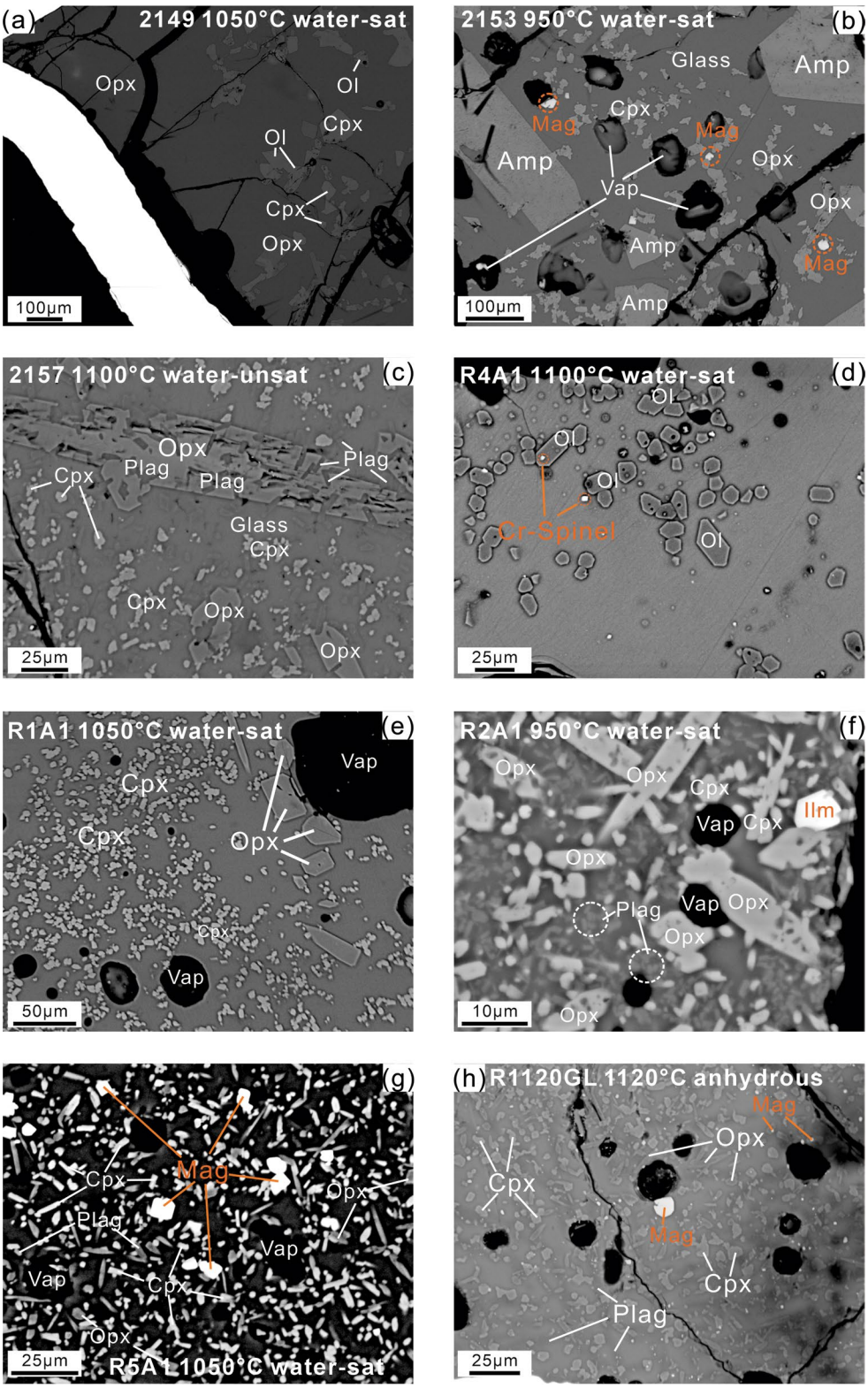

Fig. 1 Representative BSE images of experimental products using the glass starting material. **a** RUN2149 (1050 °C, 500 MPa, water-saturated); **b** RUN2153 (950 °C, 500 MPa, water-saturated) contains large irregular amphibole grains and smaller cubes of magnetite; **c** RUN2157 (1100 °C, 500 MPa, water-undersaturated) has elongated orthopyroxene crystal containing euhedral plagioclase inclusions; **d** R4A1 (1100 °C, 200 MPa, water-saturated) with euhedral olivine and Cr-spinel; **e** R1A1 (1050 °C, 200 MPa, water-saturated); **f** R2A1 (950 °C, 200 MPa, water-saturated); **g** R5A1 (1000 °C, 200 MPa, water-saturated, ΔNNO+2) containing multiple small magnetite grains; **h** R1120GL (1120 °C, 1 atm). The bubble-like pores are probably a product of the polythene oxide that was used as a binder. Phase abbreviations: *Ol* olivine, *Cpx* clinopyroxene, *Opx* orthopyroxene, *Plag* lagioclase, *Cr-spinel* chromite, *Mag* magnetite, *Ilm* lmenite, *Vap* vapour

is characterised by more euhedral form and larger dimensions (30–250 μm diameter; Fig. 1e, f) and is sometimes large enough to host inclusions of glass and other minerals (Fig. 1c). Clinopyroxene typically forms smaller (10–50 μm diameter) crystals that occur either as individual crystals or as aggregates of rounded form. Plagioclase occurs as small lath-shaped crystals (<20 μm) both within the glass matrix and as inclusions in larger orthopyroxene grains (Fig. 1c).

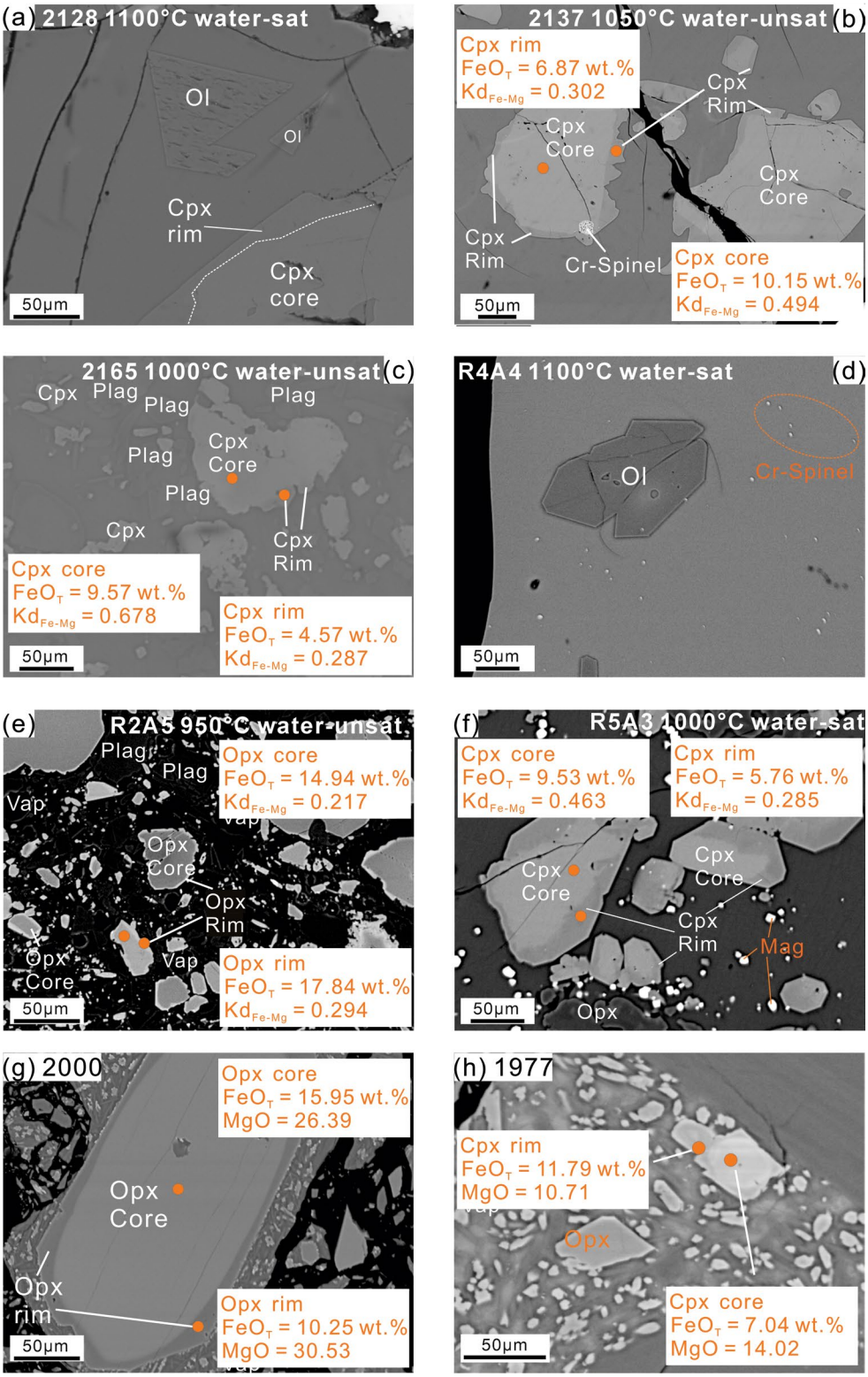

Fig. 2 BSE images of experimental products from runs on unfused rock powders. For comparison, images are also provided for the original rock (TRW34) used to make the experimental starting materials. **a** RUN2128 (1100 °C, 500 MPa, water-saturated) contains subhedral olivine crystals and anhedral clinopyroxene crystals with core-rim texture; **b** RUN2137 (1050 °C, 500 MPa, water-undersaturated) shows clear core-rim textures in both clinopyroxene and orthopyroxene crystals with relict Cr-spinel. The dimmer rim typically contains lower FeO concentration than the brighter core domain; **c** RUN2165 (1000 °C, 500 MPa, water-saturated); **d** R4A4 (1100 °C, 200 MPa, water-saturated) produces large olivine crystals and small Cr-spinel crystals; **e** R2A5 (950 °C, 200 MPa, water-undersaturated) develops Fe-rich rim compared to the core in clinopyroxene and orthopyroxene grains, and reaches water-saturation; **f** R5A3 (1000 °C, 200 MPa, water-saturated, ΔNNO+2) with core-rim textures in clinopyroxene and orthopyroxene and newly-crystallised, euhedral magnetite; **g** Large orthopyroxene phenocrysts in sample WI05 that erupted in 2000; **h** Clinopyroxene phenocrysts in sample TRW34 that erupted in 1977. Phase abbreviations can be found in Fig. 1. K_d(Fe–Mg) values were calculated using estimated ferric iron (Fe^{3+}) in minerals and glasses based on methods of Droop (1987) and Kress and Carmichael (1991), respectively

Magnetite and ilmenite were observed separately and not found together. The growth of magnetite before silicate minerals was favoured both by water-saturated conditions and higher fO_2. Both oxides typically nucleate inside the melt phase (glass) and occur as small (10–30 µm) angular to sub-rounded crystals. Amphibole was only produced in one experiment at 500 MPa (RUN2153) where it formed crystals of varying shapes and size (30–300 µm maximum diameter) (Fig. 1b). Some of the larger examples host melt and mineral inclusions.

Table 3 Averaged compositions of experimental phases determined by SEM-EDS (in wt%)

Run	T (°C)	P^a	N^b	SiO_2	TiO_2	Al_2O_3	Cr_2O_3	FeO*	MnO	MgO	CaO	Na_2O	K_2O	P_2O_5	Total[c]
Glass starting material															
500 MPa water-saturated															
RUN2159	1100	Gl	22	59.07 (09)	0.68 (03)	14.50 (07)	0.17 (02)	6.06 (05)	0.1 (02)	6.60 (05)	8.16 (06)	2.90 (04)	1.43 (03)	0.3 (03)	91.52
		Ol	10	39.77 (04)	-[e]	-	0.07 (03)	11.67 (13)	0.2 (02)	47.33 (11)	0.17 (01)	-	-	-	99.20
		Cpx	22	53.57 (8)	0.22 (07)	1.33 (32)	0.91 (13)	4.36 (35)	0.12 (04)	19.74 (86)	18.43 (85)	0.22 (05)	-	0.04 (04)	98.94
		Opx	26	55.79 (86)	0.11 (03)	1.06 (03)	0.45 (1)	7.37 (17)	0.21 (04)	31.73 (63)	2.30 (19)	0.06 (03)	-	0.06 (05)	99.13
RUN2149	1050	Gl	18	60.31 (43)	0.74 (03)	15.85 (27)	0.1 (01)	6.00 (01)	0.08 (06)	5.47 (16)	7.82 (09)	2.78 (09)	1.59 (09)	0.16 (17)	92.82
		Ol	18	39.07 (59)	0.02 (03)	-	0.03 (04)	17.49 (7)	0.27 (04)	42.35 (7)	0.20 (02)	0.06 (05)	-	0.07 (06)	99.71
		Cpx	31	52.65 (8)	0.30 (07)	1.57 (03)	0.75 (33)	5.8 (35)	0.14 (05)	17.78 (7)	19.88 (77)	0.22 (05)	-	0.06 (04)	99.19
		Opx	21	55.09 (64)	0.15 (03)	1.10 (27)	0.30 (06)	10.87 (33)	0.24 (03)	29.43 (47)	2.21 (37)	0.09 (04)	-	0.05 (05)	99.52
RUN2152	1000	Gl	20	61.73 (34)	0.74 (05)	16.71(2)	-	5.40 (3)	0.05 (07)	3.61 (13)	6.92 (2)	2.99 (11)	1.86 (05)	-	91.84
		Cpx	24	52.28 (88)	0.54 (17)	2.65 (63)	0.66 (2)	6.07 (44)	0.14 (05)	16.45 (63)	20.85 (93)	0.18 (04)	-	0.05 (07)	99.89
		Opx	18	54.48 (57)	0.17 (05)	1.31 (28)	0.18 (04)	12.75 (23)	0.30 (04)	28.03 (04)	1.82 (19)	0.03 (02)	-	0.08 (06)	99.17
RUN2153	950	Gl	30	65.77 (79)	0.48 (09)	17.03 (48)	-	3.31 (15)	0.06 (06)	2.32 (18)	5.91 (27)	3.01 (13)	2.07 (09)	0.02 (04)	89.93
		Cpx	28	51.20 (89)	0.39 (14)	2.67 (76)	0.17 (18)	7.47 (87)	0.24 (04)	16.55 (81)	20.23 (84)	0.18 (05)	0.04 (02)	-	99.13
		Opx	18	52.65 (65)	0.31 (06)	2.98 (62)	0.02 (02)	15.53 (65)	0.32 (04)	26.54 (67)	1.81 (37)	0.01 (01)	0.03 (02)	-	100.53
		Amp	24	45.03 (98)	1.54 (36)	10.82 (91)	-	**10.16 (1.2)**	0.15 (02)	16.04 (98)	11.67 (74)	1.63 (12)	0.45 (07)	-	97.48
		Mag	21	0.22 (07)	2.48 (39)	5.20 (4)	0.49 (17)	**83.37 (1.2)**	0.35 (05)	5.26 (36)	0.16 (06)	-	-	-	91.58
500 MPa water-undersaturated															
RUN2156	1150	Gl	16	60.04 (12)	0.76 (02)	16.26 (15)	-	5.57 (06)	0.10 (04)	4.56 (13)	8.05 (13)	2.93 (07)	1.73 (03)	-	97.52
		Cpx	16	52.96 (45)	0.33 (03)	2.82 (16)	0.49 (22)	5.97 (29)	0.17 (05)	18.52 (48)	18.42 (64)	0.21 (04)	0.01 (04)	0.02 (04)	99.90
		Opx	33	55.33 (64)	0.16 (05)	1.67 (52)	0.22 (06)	10.12 (28)	0.25 (03)	29.84 (51)	2.51 (21)	0.03 (04)	-	0.01 (03)	100.17
RUN2157	1100	Gl	18	62.55 (62)	0.82 (04)	16.55 (3)	-	5.40 (19)[d]	0.04 (05)	3.04 (1)	6.41 (22)	3.07 (14)	2.11 (06)	-	98.06
		Cpx	28	53.70 (68)	0.54 (08)	2.64 (39)	0.15 (15)	4.13 (84)	0.25 (04)	19.11 (67)	18.41 (44)	0.26 (06)	0.09 (05)	-	99.29
		Opx	28	54.81 (48)	0.33 (04)	2.51 (32)	0.18 (06)	7.58 (83)	0.29 (03)	31.06 (55)	2.14 (23)	0.02 (05)	-	-	98.91
		Plag	19	53.93	-	28.11	-	0.43	-	0.72	12.15	4.03	0.31		99.68
RUN2158	1050	Gl	15	66.40 (36)	0.87 (04)	15.50 (52)	-	4.15 (66)[d]	0.05 (02)	2.09 (34)	4.83 (56)	3.31 (14)	2.35 (18)	0.44 (03)	96.05
		Cpx	18	53.25 (59)	0.69 (06)	2.55 (3)	0.16 (17)	5.27 (55)	0.25 (04)	18.16 (41)	18.52 (46)	0.27 (04)	0.09 (05)	-	99.21
		Opx	21	54.22 (42)	0.43 (05)	2.75 (41)	0.17 (04)	10.24 (75)	0.32 (04)	28.5 (8)	2.18 (25)	0.12 (09)	-	0.04 (11)	98.96
		Plag[d]	16	51.96	-	30.41	-	0.09	-	0.30	12.78	4.16	0.07		99.77
RUN2163	1000	Gl	13	69.80 (98)	0.79 (07)	14.53 (56)	-	2.37 (37)	0.03 (01)	1.66 (64)	4.02 (8)	2.56 (13)	4.19 (36)	0.01 (02)	97.46
200 MPa water-saturated															
R4A1	1100	Gl	21	59.68 (18)	0.69 (03)	14.66 (15)	-	5.99 (07)	0.14 (03)	6.12 (11)	8.70 (11)	2.50 (03)	1.52 (03)	-	96.77
		Ol	16	40.05 (12)	0.02 (01)	0.20 (13)	0.03 (03)	11.47 (13)	0.23 (03)	48.85 (13)	0.26 (06)	-	-	-	101.12
		Spl	4	-	1.50	12.25	51.12	26.13	0.15	8.30	0.14	-	-	-	93.22
R1A1	1050	Gl	13	60.60 (19)	0.75 (03)	16.64 (11)	-	5.51 (08)	0.12 (03)	4.05 (06)	7.58 (08)	2.91 (04)	1.86 (02)	-	95.52
		Cpx	17	53.38 (4)	0.30 (04)	1.17 (02)	0.26 (05)	5.83 (22)	0.22 (04)	17.96 (52)	19.51 (56)	0.22 (07)	0.11 (05)	-	98.97
		Opx	16	55.26 (79)	0.19 (04)	0.87 (01)	0.22 (09)	10.40 (34)	0.28 (03)	30.52 (47)	2.14 (22)	-	-	-	100.41
R3A1	1000	Gl	16	62.45 (12)	0.80 (03)	16.91 (1)	-	5.26 (05)	0.11 (02)	2.74 (05)	6.50 (13)	3.06 (07)	2.16 (02)	-	94.69
		Cpx	14	52.85 (28)	0.48 (04)	3.88 (19)	0.10 (02)	7.36 (11)	0.24 (02)	15.93 (11)	18.35 (37)	0.38 (04)	0.22 (02)	-	99.79

Table 3 (continued)

Run	T (°C)	P^a	N^b	SiO_2	TiO_2	Al_2O_3	Cr_2O_3	FeO*	MnO	MgO	CaO	Na_2O	K_2O	P_2O_5	Total[c]
		Opx	12	53.99 (68)	0.24 (02)	2.40 (29)	0.14 (03)	13.13 (27)	0.30 (02)	27.26 (28)	2.17 (15)	-	0.05 (03)	-	99.57
		Plag	10	50.67		30.34		0.23	0.01	0.07	15.11	3.51	0.17	-	100.11
R5A1	1000	Gl	10	63.56 (89)	0.72 (05)	17.22 (41)		3.98 (09)	0.10 (03)	3.07 (27)	6.15 (3)	3.11 (21)	2.09 (04)	-	96.69
		Cpx	12	52.20 (32)	0.60 (04)	5.21 (19)	0.06 (03)	6.00 (16)	0.22 (02)	16.32 (35)	18.89 (64)	0.49 (04)	0.24 (04)	-	100.23
		Opx	13	54.67 (58)	0.27 (03)	3.71 (76)	0.17 (08)	8.72 (81)	0.27 (02)	28.94 (86)	2.24 (26)	0.14 (12)	0.21 (13)	-	99.34
		Plag	8	49.35		31.35		0.50		0.81	14.44	3.10	0.44	-	99.99
		Mag	21	-	1.87 (1)	6.39 (61)	1.56 (39)	89.45 (7)	0.41 (03)	-	0.33 (12)	-	-	-	91.84
R2A1	950	Gl	17	68.35 (47)	0.91 (04)	15.81 (19)	-	3.51 (28)	0.07 (02)	1.34 (25)	3.94 (13)	2.87 (44)	3.18 (09)	0.01 (02)	93.64
		Cpx	6	52.26 (69)	0.74 (04)	4.01 (75)	0.10 (02)	8.79 (02)	0.20 (04)	14.43 (92)	18.17 (48)	0.44 (11)	0.26 (11)	-	99.40
		Opx	46	52.87 (56)	0.43 (05)	2.81 (71)	0.11 (04)	16.78 (63)	0.32 (04)	23.93 (75)	2.24 (3)	0.11 (12)	0.09 (08)	-	99.72
		Plag	13	53.90		27.89		0.62		0.49	12.62	3.92	0.50	-	99.94
		Ilm	11	0.44 (27)	49.24 (2)	0.40 (08)	0.44 (06)	43.24 (18)	0.42 (02)	5.46 (1)	0.31 (04)	0.02 (01)	0.06 (03)	-	99.09
200 MPa water-undersaturated															
R4A2	1100	Gl	12	60.49 (1)	0.75 (03)	16.81 (1)	-	4.88 (15)	0.12 (01)	4.30 (04)	7.78 (07)	3.05 (07)	1.82 (02)	-	97.59
		Cpx	11	53.74 (62)	0.27 (02)	2.21 (15)	0.24 (04)	5.75 (24)	0.22 (02)	19.74 (34)	18.33 (38)	0.25 (08)	0.08 (03)	-	100.63
		Opx	13	54.98 (64)	0.19 (03)	1.90 (49)	0.24 (07)	9.47 (27)	0.25 (02)	30.83 (54)	2.40 (25)	-	0.04 (02)	-	100.21
R4A3 (1 wt%)	1100	Gl	12	65.41 (76)	1.01 (04)	15.74 (24)	-	3.52 (43)	0.09 (02)	2.76 (17)	5.59 (32)	3.26 (17)	2.62 (15)	-	98.11
		Cpx	13	53.81 (53)	0.41 (05)	3.14 (58)	0.15 (05)	8.08 (23)	0.25 (03)	20.27 (66)	12.98 (89)	0.30 (08)	0.12 (11)	-	99.51
		Opx	11	54.57 (26)	0.19 (03)	1.72 (25)	0.24 (07)	9.44 (31)	0.25 (02)	30.59 (42)	2.42 (29)	-	0.03 (01)	-	99.44
R1A2	1050	Gl	11	65.58 (58)	0.98 (05)	15.76 (4)	-	4.18 (32)	0.09 (03)	2.17 (18)	5.25 (33)	3.27 (17)	2.75 (09)	-	97.24
		Cpx	14	53.54 (41)	0.48 (07)	2.36 (53)	0.13 (04)	8.73 (81)	0.26 (04)	18.03 (98)	15.10 (88)	0.35 (16)	0.14 (17)	-	99.10
		Opx	15	55.34 (21)	0.19 (04)	0.87 (01)	0.22 (09)	10.38 (32)	0.28 (03)	30.46 (35)	2.15 (23)	-	-	-	99.88
		Plag	9	52.79		27.98		0.0	0.03	0.62	14.50	3.14	0.34	-	100.56
R1A3 (1 wt%)	1050	Gl	8	70.01 (46)	1.26 (05)	13.53 (32)	0.01 (01)	3.09 (14)	0.05 (02)	1.74 (26)	3.58 (27)	2.78 (06)	3.89 (14)	0.06 (04)	96.07
R3A2	1000	Gl	8	67.32 (88)	1.05 (08)	14.84 (59)		3.52 (3)	0.06 (07)	2.09 (02)	5.06 (74)	3.10 (2)	2.96 (22)	-	94.10
		Cpx	6	53.24 (57)	0.72 (03)	1.71 (03)	0.04 (03)	10.1 (6)	0.28 (03)	19.2 (61)	14.68 (42)	0.3 (02)	-	-	100.07
		Opx	10	54.22 (42)	0.43 (03)	1.77 (02)	0.14 (03)	15.32 (05)	0.32 (02)	26.23 (29)	2.16 (15)	0.08 (08)	-	-	100.67
		Plag	7	52.90		29.06		0.51		0.38	12.74	4.00	0.43	-	99.56
R5A2	1000	Gl	15	67.70 (8)	0.63 (09)	13.11 (42)	-	4.10 (44)	0.02 (06)	3.68 (41)	5.48 (62)	2.32 (17)	2.96 (34)	-	95.15
	Mag (High Ti)		8	-	29.42	3.01	0.46	62.09	0.27	3.56	1.17	-	-	-	94.40
	Mag (Low Ti)		5	-	7.08	3.38	3.46	80.17	0.19	4.97	0.74	-	-	-	92.37
R2A2	950	Gl	6	70.47	0.74	13.54	-	2.46	0.02	2.76	4.21	2.40	3.40	-	94.88
		Ilm	5	-	51.90 (2)	-	0.63 (06)	40.26 (21)	0.38 (03)	6.44 (35)	0.39 (03)	-	-	-	98.16
1 atm anhydrous															
R1220GL	1220	Gl	14	58.87 (53)	0.63 (03)	13.46 (41)	0.01 (02)	6.88 (11)	0.14 (03)	7.89 (12)	8.42 (09)	2.41 (04)	1.41 (02)	-	99.90
		Opx	10	56.48 (57)	0.15 (04)	1.09 (62)	0.20 (1)	6.65 (94)	0.23 (04)	33.62 (87)	1.57 (18)	0.01 (01)	0.04 (02)	-	100.12
R1180GL	1180	Gl	12	59.16 (49)	0.67 (03)	14.12 (55)	-	6.65 (18)	0.14 (03)	6.38 (59)	8.89 (18)	2.53 (07)	1.48 (05)	-	101.27
		Opx	11	55.07 (48)	0.13 (03)	2.16 (47)	0.31 (01)	6.33 (43)	0.20 (02)	33.11 (65)	2.09 (14)	-	-	-	99.45

Table 3 (continued)

Run	T (°C)	P^a	N^b	SiO_2	TiO_2	Al_2O_3	Cr_2O_3	FeO*	MnO	MgO	CaO	Na_2O	K_2O	P_2O_5	Total[c]
R1150GL	1150	Gl	10	58.33 (09)	0.69 (03)	14.70 (09)	-	6.86 (09)	0.14 (03)	6.34 (06)	8.83 (05)	2.61 (02)	1.47 (03)	-	98.84
		Opx	10	55.38 (54)	0.11 (05)	1.64 (69)	0.39 (15)	6.80 (32)	0.23 (03)	33.20 (99)	1.98 (35)	-	-	0	99.78
R1120GL	1120	Gl	34	64.35 (71)	0.97 (06)	13.16 (36)	0.01 (02)	6.64 (27)	0.12 (03)	3.20 (17)	6.33 (21)	2.90 (09)	2.40 (06)	0.01 (01)	98.56
		Cpx	18	51.17 (91)	0.44 (07)	3.58 (67)	0.03 (03)	7.77 (6)	0.24 (03)	17.33 (73)	18.11 (39)	0.27 (05)	0.08 (03)	-	99.01
		Opx	14	54.67 (68)	0.24 (03)	3.22 (72)	0.08 (04)	8.98 (76)	0.27 (04)	28.50 (68)	2.53 (18)	0.10 (06)	0.18 (1)	-	98.77
		Plag	28	53.38	-	28.12	-	0.51	-	0.84	13.14	3.82	0.20	-	100.32
		Mag	11	0.19 (11)	2.43 (09)	4.47 (11)	4.57 (39)	80.95 (49)	0.27 (04)	6.66 (16)	0.24 (03)	-	-	-	89.94
Unfused whole rock powder starting material															
500 MPa water-saturated															
RUN2128	1100	Gl	31	59.89 (38)	0.69 (03)	14.58 (35)	0.18 (03)	5.85 (21)	0.10 (02)	5.86 (43)	8.34 (27)	2.83 (12)	1.41 (07)	0.27 (05)	91.37
		Ol	38	39.98 (52)			0.06 (03)	13.83 (51)	0.21 (02)	45.77 (77)	0.21 (07)		-	-	100.21
	Cpx core		8	53.51 (51)	0.50 (03)	1.75 (14)	0.49 (02)	9.26 (41)	0.17 (03)	16.44 (07)	19.16 (07)	0.23 (02)	-	-	101.55
	Cpx rim		12	54.40 (61)	0.28 (04)	1.38 (22)	1.38 (11)	4.57 (16)	0.09 (02)	18.85 (45)	19.62 (49)	0.19 (03)	-	-	100.78
		Sp	4	-	**1.42 (1.9)**	11.82 (66)	**48.41 (7.2)**	**27.04 (3.9)**	0.20 (16)	10.48 (37)	0.15 (03)	0.03 (02)	-	-	96.78
RUN2127	1050	Gl	18	60.75 (23)	0.73 (03)	17.90 (15)	0.12 (03)	4.70 (22)	0.07 (02)	3.26 (17)	6.78 (17)	3.61 (11)	1.77 (08)	0.32 (04)	94.97
	Cpx core		9	52.69 (64)	0.50 (07)	1.80 (07)	0.53 (11)	9.49 (68)	0.21 (03)	16.36 (34)	18.43 (37)	0.25 (02)	-	-	100.29
	Cpx rim		8	52.44 (6)	0.60 (08)	3.54 (22)	0.63 (06)	6.68 (44)	0.12 (03)	17.57 (57)	18.22 (54)	0.25 (02)	-	-	100.08
	Opx core		13	54.11 (24)	0.23 (03)	1.01 (07)	0.16 (04)	15.55 (58)	0.32 (03)	26.21 (46)	2.05 (05)	0.06 (02)	-	-	99.75
	Opx rim		7	54.57 (29)	0.20 (02)	1.81 (58)	0.24 (05)	11.51 (6)	0.22 (03)	28.59 (45)	2.08 (09)	0.05 (01)	-	-	99.28
RUN2129	1000	Gl	19	65.01 (1)	1.11 (03)	15.01 (08)		5.43 (14)	0.09 (02)	1.98 (06)	5.00 (07)	3.43 (04)	3.00 (03)	-	97.30
	Cpx core		11	52.39 (4)	0.76 (05)	2.63 (68)	0.10 (04)	7.54 (71)	0.24 (03)	17.25 (45)	18.57 (28)	-	-	-	99.48
	Cpx rim		10	51.82 (63)	0.49 (1)	1.90 (13)	0.05 (07)	9.32 (64)	0.26 (02)	16.06 (72)	18.92 (19)	-	-	-	99.50
	Opx core		8	54.49 (16)	0.20 (05)	1.10 (33)	0.23 (15)	13.19 (81)	0.28 (02)	28.53 (66)	2.11 (17)	-	-	-	100.13
	Opx rim		9	53.99 (35)	0.27 (04)	1.11 (26)	0.11 (02)	15.51 (35)	0.33 (03)	26.57 (47)	2.24 (21)	-	-	-	100.12
		Plag	8	51.88 (73)	-	30.21 (83)				0.18 (03)	13.24 (59)	3.73 (03)	0.35 (04)	-	99.59
500 MPa water-undersaturated															
RUN2138	1150	Gl	17	59.72 (13)	0.74 (03)	15.35 (08)	-	6.30 (06)	0.04 (06)	4.98 (05)	8.21 (06)	2.90 (05)	1.76 (03)	-	97.81
	Cpx core		12	52.57 (23)	0.47 (03)	1.69 (05)	0.08 (08)	9.50 (15)	0.26 (01)	15.86 (19)	18.93 (21)	-	-	-	99.35
	Cpx rim		11	53.95 (31)	0.26 (03)	2.55 (24)	0.58 (08)	5.97 (13)	0.12 (09)	18.36 (37)	18.21 (4)	-	-	-	100.17
	Opx core		14	54.28 (94)	0.23 (03)	1.05 (07)	0.15 (03)	15.97 (65)	0.33 (02)	25.48 (82)	2.09 (06)	-	-	-	99.51
	Opx rim		8	55.83 (31)	0.12 (01)	1.30 (45)	0.38 (07)	9.87 (34)	0.21 (02)	29.47 (27)	2.47 (04)	-	-	-	99.57
RUN2137	1100	Gl	13	59.85 (29)	0.71 (04)	17.41 (04)		5.15 (09)	0.12 (03)	4.77 (14)	7.71 (16)	3.13 (05)	1.85 (04)	-	96.31
	Cpx core		11	52.51 (52)	0.46 (06)	1.83 (07)	0.17 (06)	9.41 (5)	0.26 (04)	16.93 (37)	19.04 (28)	0.21 (04)	0.01 (01)	-	100.73
	Cpx rim		10	52.40 (66)	0.41 (06)	3.07 (59)	0.37 (08)	6.54 (24)	0.18 (03)	17.96 (47)	18.77 (47)	0.21 (03)	0.02 (02)	-	99.80
	Opx core		7	53.76 (42)	0.30 (07)	1.09 (39)	0.12 (06)	15.91 (67)	0.34 (02)	26.63 (72)	2.14 (32)	0.01 (01)	-	-	100.16
	Opx rim		12	54.34 (51)	0.24 (05)	2.33 (44)	0.29 (09)	10.78 (34)	0.29 (03)	29.14 (5)	2.31 (13)	-	0.03 (01)	-	99.65
RUN2165	1050	Gl	23	67.56 (79)	1.13 (07)	15.18 (24)	0.13 (05)	3.23 (37)	0.03 (03)	1.71 (14)	4.18 (32)	3.46 (1)	2.92 (12)	0.45 (07)	96.88
	Cpx core		12	53.13 (15)	0.89 (09)	2.73 (48)	0.53 (04)	5.78 (84)	0.22 (03)	17.65 (34)	18.03 (39)	0.36 (06)	0.09 (07)	0.12 (04)	99.89
	Cpx rim		14	51.74 (37)	0.55 (05)	2.11 (15)	0.61 (14)	9.04 (97)	0.16 (05)	15.98 (49)	18.43 (49)	0.24 (03)		0.10 (04)	99.24
	Opx core		9	56.65 (27)	0.37 (02)	1.76 (39)	0.07 (02)	7.50 (32)	0.37 (04)	29.12 (74)	2.00 (14)	0.19 (06)	0.24 (09)	0.10 (05)	98.38

Table 3 (continued)

Run	T (°C)	P^a	N^b	SiO_2	TiO_2	Al_2O_3	Cr_2O_3	FeO*	MnO	MgO	CaO	Na_2O	K_2O	P_2O_5	Total[c]
	Opx rim		13	54.34 (73)	0.26 (05)	1.11 (03)	0.19 (1)	15.78 (6)	0.33 (05)	26.11 (24)	2.18 (05)	0.03 (05)	-	0.13 (02)	100.46
		Plag	14	49.06	-	31.46	0.27 (03)	0.71	0.01	0.09	15.26	2.88	0.15	-	99.62
200 MPa water-saturated															
R4A4	1100	Gl	17	59.16 (31)	0.66 (03)	14.20 (16)	-	6.54 (06)	0.13 (02)	6.59 (06)	8.70 (12)	2.50 (05)	1.51 (02)	-	97.09
		Ol	18	39.97 (46)	0.01 (03)	-	0.03 (02)	12.01 (34)	0.20 (03)	48.71 (51)	0.20 (03)	-	-	-	100.88
		Spl	5	-	0.78	8.27	49.08	29.65	0.20	11.94	-	-	-	-	92.45
R1A4	1050	Gl	14	60.26 (16)	0.73 (04)	16.09 (06)	-	6.08 (08)	0.13 (03)	4.56 (03)	7.55 (09)	2.89 (05)	1.75 (02)	-	96.04
		Ol	16	39.25 (46)	-	-	0.03 (02)	14.59 (51)	0.24 (02)	46.40 (45)	0.16 (01)	-	-	-	100.60
	Cpx core		30	51.72 (19)	0.46 (08)	1.77 (18)	0.17 (1)	9.36 (64)	0.25 (04)	16.59 (34)	18.85 (27)	0.20 (03)	0.01 (01)	-	99.43
	Cpx rim		32	52.43 (23)	0.22 (05)	1.65(18)	0.46 (09)	5.05 (15)	0.17 (03)	18.17 (32)	20.82 (34)	0.16 (04)	0.02 (02)	-	99.17
R3A4	1000	Gl	16	60.15 (23)	0.75 (02)	17.77 (12)	-	5.49 (08)	0.10 (02)	3.62 (06)	7.07 (07)	3.14 (03)	1.92 (03)	-	95.13
	Cpx core		13	52.06 (36)	0.48 (06)	1.88 (15)	0.06 (08)	9.62 (59)	0.25 (03)	16.42 (04)	18.95 (31)	0.03 (04)	-	-	99.92
	Cpx rim		10	52.33 (4)	0.37 (05)	2.51 (45)	0.25 (08)	6.31 (52)	0.16 (03)	17.09 (44)	20.97 (66)	0.17 (03)	0.05 (04)	-	100.08
	Opx core		16	53.08 (24)	0.23 (03)	1.04 (03)	0.11 (04)	15.73 (76)	0.34 (05)	26.67 (6)	2.09 (03)	0.02 (01)	-	-	98.87
	Opx rim		15	54.27 (23)	0.17 (13)	1.59 (31)	0.20 (04)	10.98 (5)	0.23 (02)	30.23 (61)	1.46 (16)	0.02 (04)	0.03 (05)	-	99.22
R5A3	1000	Gl	9	61.73 (24)	0.71 (05)	17.52 (09)	-	4.26 (1)	0.10 (02)	3.73 (07)	6.92 (07)	3.17 (04)	1.94 (03)	-	95.55
	Cpx core		24	51.31 (24)	0.45 (06)	1.85 (11)	0.06 (06)	9.53 (71)	0.26 (03)	16.23 (43)	18.79 (32)	0.24 (03)	0.02 (02)	-	98.76
	Cpx rim		17	50.49 (63)	0.43 (07)	3.69 (56)	0.03 (05)	5.76 (34)	0.18 (02)	16.72 (43)	21.58 (78)	0.29 (09)	0.06 (05)	-	99.22
		Plag	12	55.40 (57)	0.15 (03)	1.94 (5)	0.10 (05)	6.29 (48)	0.27 (02)	34.66 (39)	1.24 (07)	0.02 (03)	0.03 (02)	-	100.12
		Mag	13	-	1.46 (06)	5.78 (56)	0.67 (51)	81.15 (1.4)	0.37 (03)	9.80 (64)	0.22 (1)	-	-	-	91.47
R2A4	950	Gl	12	63.91 (07)	0.83 (02)	17.45 (05)	-	4.54 (07)	0.07 (02)	1.87 (02)	5.03 (03)	3.80 (05)	2.51 (03)	0.02 (03)	95.45
	Cpx core		13	52.15 (68)	0.67 (08)	1.19 (01)	-	8.48 (59)	0.21 (02)	15.48 (26)	21.12 (73)	0.26 (09)	-	-	99.56
	Cpx rim		10	52.16 (32)	0.48 (12)	1.90 (23)	0.07 (02)	10.69 (76)	0.34 (02)	16.06 (43)	18.92 (56)	0.17 (05)	0.03 (01)	-	100.58
	Opx core		12	54.24 (42)	0.23 (04)	1.51 (52)	0.25 (1)	12.75 (88)	0.25 (04)	28.88 (5)	2.13 (18)	-	0.02 (01)	-	100.12
	Opx rim		6	53.60 (12)	0.24 (01)	0.76 (01)	0.06 (03)	16.35 (05)	0.31 (01)	27.11 (47)	1.33 (01)	-	-	-	99.76
		Plag	11	46.66 (56)	0.05 (03)	33.37 (41)	-	0.75 (01)	0.02 (02)	0.07 (02)	16.47 (46)	2.00 (21)	0.17 (06)	-	99.56
		Mag	10	-	9.55 (57)	**8.40 (1.8)**	**3.72 (1.1)**	71.28 (2.6)	0.31 (04)	6.62 (2.70)	-	-	-	-	92.28
200 MPa water-undersaturated															
R4A5	1100	Gl	11	59.99 (24)	0.83 (08)	16.02 (26)	-	5.46 (43)	0.11 (05)	4.82 (09)	8.21 (2)	2.71 (08)	1.83 (07)	0.03 (04)	92.02
	Cpx core		12	51.81 (25)	0.46 (06)	1.77 (12)	-	9.65 (91)	0.27 (04)	16.04 (43)	19.61 (33)	0.17 (03)	-	-	99.77
	Cpx rim		14	52.76 (80)	0.28 (11)	1.96 (67)	-	5.18 (60)	0.21 (03)	17.90 (72)	20.86 (45)	0.17 (03)	-	-	99.32
	Opx core		12	53.39 (49)	0.27 (04)	0.98 (04)	-	**15.77 (1.6)**	0.38 (02)	26.26 (98)	2.15 (07)	-	-	-	99.33
	Opx rim		14	56.44 (23)	0.19 (05)	1.25 (21)	-	9.02 (25)	0.26 (04)	31.77 (31)	2.10 (13)	-	-	-	101.03
R1A5	1050	Gl	15	61.61 (14)	0.85 (03)	17.25 (07)	-	4.89 (05)	0.09 (02)	3.12 (05)	6.51 (06)	3.48 (04)	2.21 (03)	-	97.57
	Cpx core		19	51.76 (26)	0.44 (06)	1.89 (12)	0.13 (07)	9.22 (95)	0.24 (04)	16.55 (5)	18.96 (42)	0.21 (03)	0.01 (02)	-	99.45
	Cpx core		20	52.02 (18)	0.38 (03)	2.52 (15)	0.15 (05)	6.30 (21)	0.18 (02)	17.38 (15)	20.19 (28)	0.18 (03)	-	-	99.22
	Opx rim		17	53.74 (42)	0.26 (1)	1.60 (35)	0.12 (06)	**13.33 (1.6)**	0.27 (05)	28.17 (91)	2.11 (27)	0.01 (01)	0.02 (01)	-	99.65
	Opx rim		16	54.36 (37)	0.26 (02)	1.83 (43)	0.13 (03)	11.89 (34)	0.25 (03)	29.61 (28)	2.03 (24)	-	0.03 (02)	-	100.24
R3A5	1000	Gl	12	64.21 (17)	1.01 (05)	16.41 (06)	-	4.83 (21)	0.09 (03)	1.98 (02)	5.08 (06)	3.60 (04)	2.78 (02)	-	97.76
		Cpx	28	51.66 (52)	0.47 (07)	1.88 (47)	0.15 (15)	9.30 (53)	0.24 (03)	16.14 (47)	19.02 (33)	0.21 (04)	0.01 (02)	-	99.08

Table 3 (continued)

Run	T (°C)	P^a	N^b	SiO_2	TiO_2	Al_2O_3	Cr_2O_3	FeO*	MnO	MgO	CaO	Na_2O	K_2O	P_2O_5	Total[c]
	Opx core		8	53.48 (34)	0.25 (02)	1.14 (22)	0.10 (03)	16.84 (76)	0.39 (05)	26.09 (45)	2.10 (14)	-	-	-	100.22
	Opx rim		10	54.63 (61)	0.26 (04)	1.29 (48)	0.16 (06)	14.26 (68)	0.31 (03)	27.52 (87)	2.41 (31)	-	-	-	100.72
		Plag	13	50.94 (72)	-	30.72 (49)	-	0.32 (21)	0.02 (02)	0.06 (08)	13.76 (48)	3.63 (25)	0.29 (05)	-	99.74
R2A5	950	Gl	15	68.74 (23)	0.79 (05)	15.25 (14)	-	3.63 (15)	0.06 (02)	0.91 (06)	3.34 (16)	3.58 (09)	3.63 (05)	0.08 (04)	98.23
	Cpx core		10	51.66 (27)	0.46 (09)	1.94 (16)	0.13 (12)	9.51 (41)	0.26 (05)	16.33 (46)	18.78 (24)	0.21 (03)	0.01 (02)	-	99.32
	Cpx rim		16	51.34 (35)	0.59 (04)	2.71 (49)	-	10.79 (29)	0.28 (02)	13.96 (28)	18.82 (73)	0.32 (06)	0.18 (05)	-	98.94
	Opx core		16	54.10 (32)	0.25 (05)	1.14 (14)	0.16 (07)	14.94 (1.1)	0.31 (03)	27.39 (78)	2.15 (08)	-	0.02 (02)	-	100.52
	Opx rim		9	53.12 (68)	0.30 (04)	1.97 (74)	0.04 (02)	17.84 (59)	0.41 (02)	23.71 (94)	1.82 (34)	0.14 (09)	0.07 (05)	-	99.45
		Plag	10	50.95 (95)	-	30.49 (98)	-	0.77 (01)	-	0.14 (06)	13.18 (95)	3.81 (53)	0.33 (06)	-	99.67
		Mag	6	0.21 (02)	42.98 (9)	**4.34 (2.3)**	0.42 (04)	44.49 (83)	0.36 (01)	5.80 (44)	1.40 (42)	-	-	-	98.97
1 atm anhydrous															
R1220M	1220	Gl	27	59.33 (72)	0.66 (06)	13.94 (52)	0.01 (03)	6.31 (56)	0.12 (03)	6.87 (62)	8.60 (49)	2.57 (18)	1.54 (12)	-	99.77
		Opx	21	53.29 (17)	0.24 (05)	1.08 (18)	0.10 (04)	15.75 (43)	0.33 (03)	26.52 (37)	2.09 (12)	-	-	0	99.49
		Plag	18	50.75 (62)	-	30.19 (41)	-	0.70 (02)	0.02 (02)	0.12 (02)	13.40 (42)	3.58 (21)	0.29 (03)	0	99.06
R1180M	1180	Gl	16	59.67 (59)	0.69 (03)	14.46 (31)	0.02 (04)	5.79 (32)	0.12 (04)	5.95 (32)	9.03 (28)	2.67 (12)	1.59 (09)	0.01 (03)	98.76
		Cpx	9	52.70 (16)	0.39 (04)	2.49 (39)	0.15 (03)	5.84 (34)	0.19 (03)	18.80 (42)	18.07 (31)	0.17 (04)	-	-	98.82
	Opx core		11	53.65 (65)	0.26 (03)	1.16 (37)	0.15 (02)	14.68 (65)	0.31 (02)	27.04 (56)	2.18 (38)	0.01 (02)	0.01 (01)	-	99.52
	Opx rim		7	55.60 (33)	0.14 (03)	1.44 (39)	0.33 (05)	7.64 (72)	0.23 (03)	32.91 (75)	2.27 (41)	0.02 (02)	-		100.67
		Plag	10	50.45 (65)	0.07 (03)	30.50 (43)	-	0.73 (04)	0.03 (02)	0.14 (03)	13.98 (46)	3.30 (2)	0.26 (04)	-	99.47
R1150M	1150	Gl	14	60.11 (58)	0.76 (05)	14.49 (24)	0.01 (01)	6.16 (42)	0.12 (03)	5.42 (34)	8.25 (44)	2.87 (07)	1.79 (11)	0.01 (01)	98.77
	Opx core		10	53.68 (12)	0.22 (06)	1.08 (2)	0.13 (07)	14.65 (63)	0.31 (03)	27.11 (53)	2.12 (01)	0.04 (01)	-	-	99.35
	Opx rim		8	56.00 (41)	0.12 (05)	1.06 (34)	0.28 (11)	6.92 (35)	0.23 (03)	33.21 (43)	2.30 (23)	0.06 (04)	-	-	100.27
		Plag	12	51.30 (83)	-	30.05 (56)	-	0.77 (04)	0.02 (02)	0.15 (03)	13.38 (58)	3.61 (28)	0.30 (04)	-	99.59
R1120M	1120	Gl	18	63.85 (84)	1.30 (16)	14.06 (38)	-	5.47 (38)	0.11 (03)	3.11 (19)	5.58 (24)	3.62 (07)	2.80 (09)	0.09 (06)	99.22
		Cpx	10	50.95 (61)	0.84 (14)	3.19 (3)	0.06 (05)	7.45 (27)	0.21 (04)	18.01 (31)	18.39 (42)	0.32 (05)	-	-	99.40
	Opx core		6	52.96 (22)	0.25 (05)	1.06 (05)	0.12 (03)	16.08 (17)	0.36 (02)	26.24 (12)	2.07 (04)	-	-	-	99.14
	Opx rim		12	54.60 (75)	0.22 (18)	1.40 (63)	0.24 (19)	9.54 (5)	0.25 (05)	31.22 (43)	2.07 (21)	-	-	-	99.57
		Plag	10	51.08 (83)	0.06 (02)	30.27 (61)	-	0.82 (08)	0.02 (02)	0.15 (02)	13.59 (6)	3.60 (3)	0.26 (04)	0	99.86
	Mag (Low Ti)		10	0.32 (05)	6.01 (29)	4.99 (12)	0.33 (03)	78.57 (85)	0.37 (03)	8.39 (4)	0.38 (04)	-	-	-	94.35
	Mag (High Ti)		7	0.36 (02)	26.29 (3)	1.47 (11)	0.15 (02)	64.59 (54)	0.15 (02)	5.57 (27)	0.47 (05)	-	-	-	97.55

Glasses have been renormalised to an anhydrous base and 100%. The numbers in bracket are standard deviations of the data used to obtain the average compositions. They are usually expressed to two decimal places, for example, 53 = 0.53, 1 = 0.1. However, for some phases (particularly magnetite), the standard deviations may be higher than 1.00 (wt%); therefore, the results are presented in their original values, and the numbers are bolded. For experiments on unfused rock powder, the rim composition presented here contains two scenarios: (1) mineral rim with appropriate K_d(Fe–Mg) ratios and (2) mineral core but also shows appropriate K_d(Fe–Mg) ratios

a: All the phase abbreviations are the same in Table 2

b: Number of individual analyses for each phase

c: Original total amount analysed by SEM-EDS. For glass composition, all the oxide concentrations reported were normalised to 100%

d: For some plagioclase, magnetite, and ilmenite compositions, the results reported here were calibrated by regression model to minimise the secondary fluorescence. The details are recommended to refer to Supplementary Materials

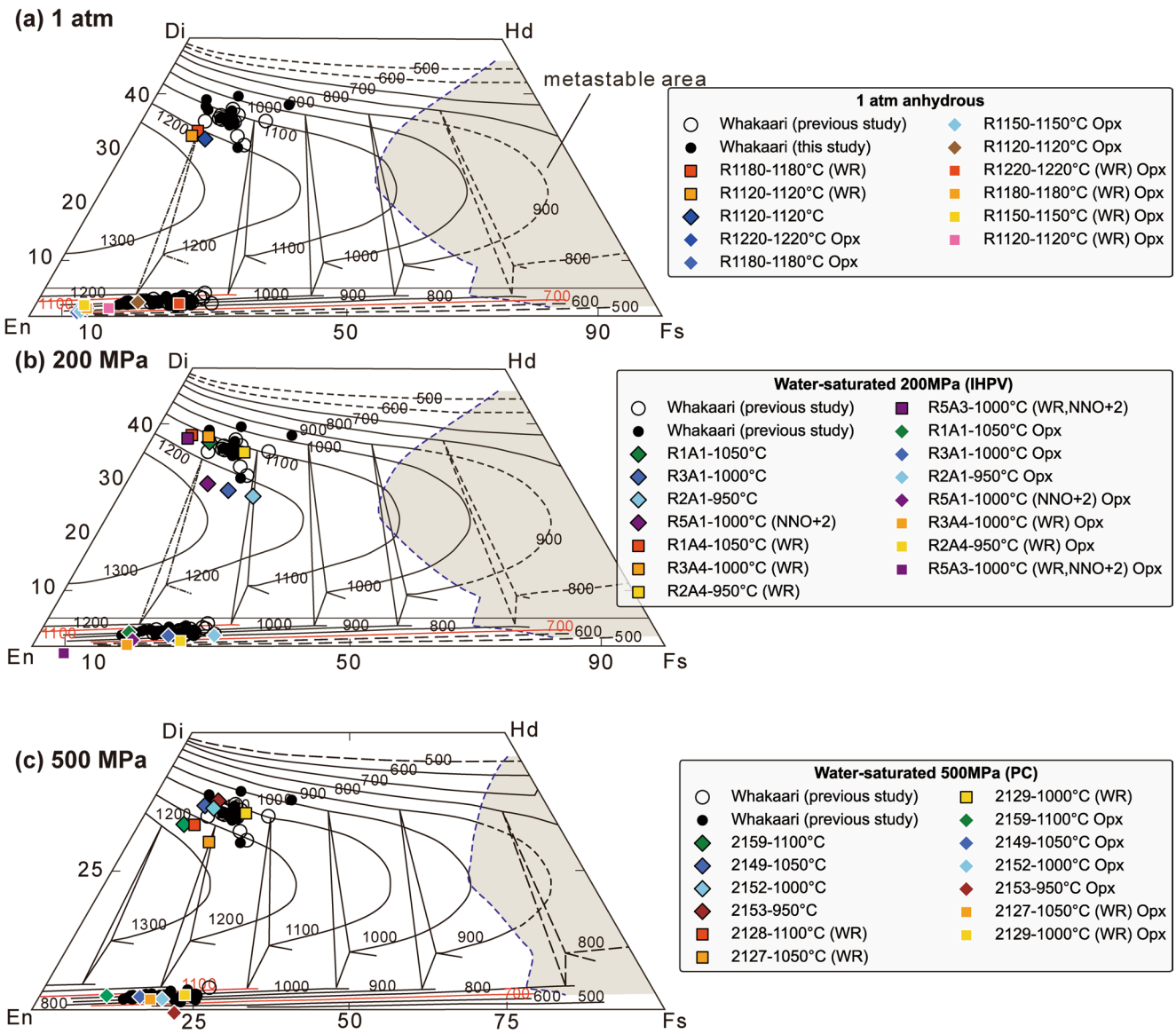

Fig. 3 Wo–En–Fs ternary diagrams for pyroxenes thermobarometer (modified after (Lindsley and Andersen 1983) showing the results from water-saturated experiments. **a** 1 atm; **b** 200 MPa; and **c** 500 MPa experiments. The red triangles and green triangles represent the modelling results at ΔNNO + 1 and NNO, respectively, with 0.5 wt% initial water concentration and 60 MPa constant pressure. The published clinopyroxene and orthopyroxene compositions are sourced from Cole and Graham (1989); Heyworth et al. (2007); Severs et al. (2009); Shiraki et al. (1994). The mineral compositions selected here for experiments on unfused rock powders are all from rim composition. All the pyroxene compositions are average values from each experiment. *Wo* wollastonite, *Fs* ferrosilite, En enstatite

For experiments on unfused rock powder, clinopyroxene and orthopyroxene typically exhibit subhedral to anhedral form with either rounded or jagged edges (Fig. 2b, c, f). They also display core-rim variations that resemble the zoning found in natural Whakaari phenocrysts, although the latter can be more complicated (Fig. 2g, h). This is evident in BSE images that show bright cores and dark rims for pyroxenes from higher temperature runs, but a reversed pattern for the lower temperature runs (< 1000 °C) (Fig. 2e). Plagioclase from experiments on unfused rock powders occurs as two separate forms. One is characterised by comparatively large (30–500 µm) and irregular crystals of rounded to sub-rounded shape, and the other as euhedral crystallites (< 10 µm) (Fig. 2c, e).

The glasses produced by experiments on both glass starting material and unfused rock powder are homogenous and often vesicular, with broadly andesitic to dacitic compositions (Fig. 2a, e, g). Some water-undersaturated experiments exhibited significant Fe-loss (20–50%), but this is less evident for water-saturated experiments and 1 atm experiments. High Fe-loss is associated with both longer run times and higher temperatures.

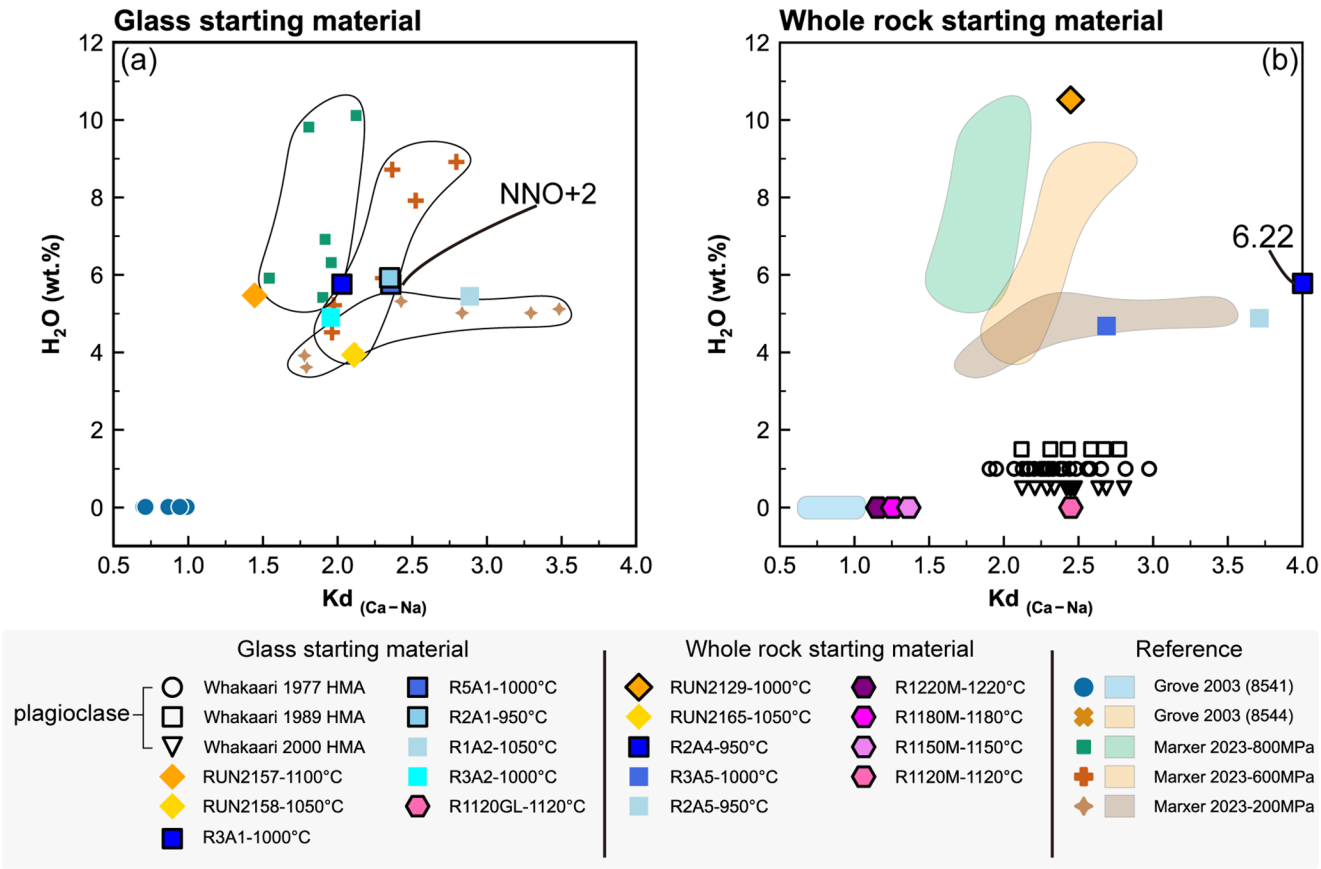

Fig. 4 The relationship between K_d(Ca–Na) ratios of experimental and natural plagioclase and melt water concentrations. **a** for experiments on glass starting materials and **b** for experiments on unfused rock powder materials. The outputs from the water-saturated experiments are enclosed in black edges, whereas those from the water-undersaturated experiments are not. All the plagioclase compositions from each experiment are average values. To facilitate comparison of plagioclase K_d(Ca–Na) ratios across natural samples, we estimated pre-eruptive water concentrations (0.5–1.5 wt%) for the three high-Mg andesites hosting these plagioclases (panel b). These K_d(Ca–Na) values were calculated using average matrix glass compositions from the respective 1977, 1989, and 2000 eruptive units. The natural plagioclase compositions are from the same sources as in Fig. 3, whereas the matrix glass compositions are from Mandon et al. (2021); Kilgour et al. (2021b). The experimental results are from Grove et al. (2003) and Marxer et al. (2023)

Mineral chemistry

The mineral compositions from the experiments are presented in Table 3. New data for natural phenocryst compositions, including spinel, ilmenite, plagioclase, clinopyroxene and orthopyroxene are listed in Tables SI 1–3.

Cr-spinel and olivine

Only two experiments at 200 MPa (R4A1 and R4A2) produced chromites that were sufficiently large for quantitative analysis by SEM-EDS (Fig. 1d; Figs. SI 2–3; Table 3). These are compositionally similar to chromites from Whakaari high-Mg andesites having Cr# ≈ 0.8 (Cr# = Cr/(Cr+Al), but are distinct from the evolved ferrian-chromites (higher Fe^{3+} concentration) and Al-rich hercynites that are also found at Whakaari (see Supplementary Materials). Fo in experimentally produced near-liquidus olivines vary from 88 to 81 and are lower than the highest Fo values (up to 92.9) (Fig. SI 5) measured in olivine phenocrysts from TRW34. CaO in the experimental olivines varies from 0.15 to 0.22 wt% which lies within the range of the natural olivine phenocrysts. The CaO contents in olivine grains were corrected using the method described in Gavrilenko et al. (2023) to minimise the secondary fluorescence effect during SEM analysis.

Pyroxenes

Clinopyroxenes crystallised during water-saturated experiments at both 200 and 500 MPa are mostly augites ($Wo_{27–38}En_{51–60}Fs_{7–21}$). On the quadrilateral projection of Lindsley and Andersen (1983), they plot close to the same 1100 °C isobar followed by phenocrysts from the high-Mg andesites (Fig. 3; Table 3). These exclude a subset of experiments that produced clinopyroxenes with distinctly lower Wo (Fig. 3; Fig. SI 6; Table 2). These were mainly

lower-temperature experiments on glass starting material where the degree of crystallisation was comparatively large. Similar observations apply to the clinopyroxenes from water-undersaturated experiments, although 500 MPa experiments consistently produced clinopyroxenes that were depleted in Wo relative to expected values (Fig. 3). Although the clinopyroxenes from 1 atm experiments are more depleted in Wo than the natural phenocrysts (Fig. 3) this is consistent with the comparatively high temperatures (~1200 °C) of anhydrous crystallisation.

The orthopyroxenes are predominantly enstatites ($Wo_{0-3}En_{70-92}Fs_{7-28}$) that become increasing Fe-rich with increasing crystallisation. As with clinopyroxene, the orthopyroxenes from experiments on unfused rock powders are characterised by distinctive overgrowths (Fig. 2). At temperatures above 1000 °C, these overgrowths exhibit lower Fe concentrations compared to pyroxene cores. However, as temperature decreases to 1000 °C or below, the pyroxene rims become enriched in Fe relative to the cores (Table 3). Similar patterns of zoning characterise pyroxene phenocrysts in the natural high-Mg andesites (Fig. 2). No zoning was evident for experiments on glass starting materials. The relict proportions, ranging from $0.36 \pm \frac{0.40}{0.19}\%$ to $46.38 \pm \frac{12.6}{9.07}\%$, are estimated by mass balance calculations.

Plagioclase

The plagioclase from experiments on glass starting materials is of calcic-labradorite to bytownite composition (An = 62.5–72.0) and duplicates the range of An in plagioclase phenocrysts from Whakaari high-Mg andesites (An = 63–74). K_d(Ca–Na) relationships for the same experiments (1.49–2.91) (where $K_d(Ca\text{-}Na) = [X_{Ca}^{plag} * X_{Na}^{liquid}]/[X_{Ca}^{liquid} * X_{Na}^{plag}]$) overlap with K_d values for Whakaari phenocrysts and matrix glasses (1.90–2.97). Kd values increase with melt-H_2O concentration (Fig. 4), as shown by samples R3A2 and R3A1, where Kd rises slightly from 2.49 wt% to 5.9 wt% H_2O (Table 2). Conversely, Kd values decrease with increasing temperature (Fig. 5). This negative temperature dependence is evident in our 200 MPa experiments comparing runs at different temperatures using identical starting materials (e.g., R3A1 vs. R2A1). These relationships are similar to those found by previous studies (Grove et al. 2003; Marxer et al. 2023) for other high-Mg arc magmas. There is no clear relationship between oxygen fugacity and plagioclase composition (see R5A1, ΔNNO + 2 and R3A1, ΔNNO + 1). Most experimental plagioclase compositions fall within the range defined by natural plagioclase from three high-Mg andesites (TRW34, 891129, WI05), except for RUN2157 (1000 °C, 500 MPa; Fig. 4a).

Plagioclases from experiments on powdered rock starting materials are generally more calcic (An = 65.66–81.99) and may persist to higher temperatures than is the case for glass starting materials. K_d(Ca–Na) relationships (1.13–6.22) are also less consistently related to changes in water content and temperature. Notably, only three experimental plagioclases, R5A3, R1120M, and RUN2129, fall within the K_d(Ca–Na) range observed in natural plagioclases. However, these results are mainly for the comparatively large and irregular plagioclase grains (probably relict) rather than the euhedral crystallites that accompanied them, the latter being too small for quantitative analysis. The anomalously high Kd value of sample R2A4 (6.22), showing clear disequilibrium with the experimental glass, reinforces this distinction.

Magnetite and Ilmenite

The experimentally produced magnetites included both high TiO_2 (26.39–29.42 wt%) and low TiO_2 variants (6.03–7.09 wt%) (Figs. SI 4) with the latter more closely resembling magnetite phenocrysts ((0.24–2.69 wt%) in the natural high-Mg andesites (Table SI 1).

Amphibole

Amphibole of edenite to pargasite composition was produced in one run (RUN 2153) under sub-liquidus, water-saturated conditions at 500 MPa. Amphibole did not crystallise in any other run.

Glasses

The compositions of experimentally produced glasses are presented in Table 3 whereas those of natural matrix glasses are shown in Table SI 3. The two sets can be compared in Figs. 6 and 7 and Figure SI 7 together with data for Whakaari melt inclusions.

It is apparent that the melt inclusions hosted by olivine form a distinct and relatively primitive group (most closely resembling whole rock compositions), whereas those in plagioclase, clinopyroxene and orthopyroxene sample a more evolved spectrum of melts. This second group is compositionally analogous to the matrix glasses, although there is more compositional scatter (attributable to a combination of variable analytical effects and post-entrapment alteration). Unsurprisingly, the experimental melts that most closely resemble the natural matrix glasses also produced plagioclase, clinopyroxene and orthopyroxene (Fig. 6; Fig. SI 7). This is most evident for experiments run under comparatively dry (with dissolved $H_2O \leq 2$ wt%) and low- pressure conditions (≤200 MPa) with fO_2 close to Ni–NiO + 1. None

of our experiments produced glasses that closely matched those of olivine-hosted melt inclusions.

Discussion

Water, Fe-loss and fO_2 variations during experiments

Fe-loss to metal sample capsules during experiments is a commonly cited problem (Barr and Grove 2010; Jakobsson 2012; Kägi et al. 2005; Matjuschkin et al. 2015) and is evident for some our own experiments, particularly those conducted at either higher temperatures and/or for longer durations. This was minimized in the case of our 1 atm runs by the pre-saturation of wire loops with Fe (Brugier et al. 2015; Kägi et al. 2005). Fe-loss from starting materials is potentially associated with a number of other effects. One of these results from hydrogen diffusion into capsules that facilitates the reduction of FeO to Fe metal while also producing H_2O. This occurs via the reaction:

$$FeO + H_2 \rightarrow Fe + H_2O \quad (2)$$

.

This produces 0.25 wt% of H_2O for every 1 wt% of FeO lost to the metal capsule as Fe metal. It can also be noted that, on the basis of reaction 2, the maximum possible gain of H_2O to starting materials is 1.75 wt% for RUN 2131 where relative Fe-loss was 100%. But for all other experiments (where relative Fe-loss was < 50%) this would have been < 0.75 wt%. To check these predictions, we also calculated melt-water concentrations for our experiments using plagioclase-melt hygrometers of (Putirka 2005; Waters and Lange 2015). However, both hygrometers provided estimates that appear to be unrealistically high (Table 2), approaching water saturation at 200 MPa. Such values are inconsistent with the relative abundance of plagioclase and high overall degree of crystallisation in nominally water-undersaturated experiments. We consider it more likely that, consistent with reaction 2, any degree of water-enrichment that accompanied Fe-loss in our experiments was comparatively small and insufficient to cause major changes in phase equilibria.

It is also possible for the reduction of iron to occur without the involvement of hydrogen. In this case, Fe-loss causes the starting material to become oxidised. Oxidation may also be produced by the diffusion of hydrogen out of water-bearing capsules (Kägi et al. 2005). Both effects will be self-limiting since oxidation of the starting material will inhibit further reduction. One possible effect of oxidation during experiments will be the promotion of magnetite crystallisation through associated increases in Fe^{3+}. Consistent with this, magnetite in our water-undersaturated 200 MPa experiments was only stabilised at $fO_2 = NNO + 2$ (R5A2; Table 2). However, the magnetite from these experiments is Ti-rich (with up to 29.42 wt% TiO_2) when compared to natural Whakaari phenocrysts (< 2.69 wt%). The magnetite proportion in R5A2 (0.6 ± 0.2%) is significantly lower than in experiments with minimal Fe-loss (> 1.2%) and natural rocks (≈ 1%). Both this depletion and TiO_2 enrichment in magnetite likely reflect compensation for substantial Fe-loss from the melt. This effect may also explain the sharp crystallinity decrease observed in our 1 atm experiments (using glass starting materials), where R1120GL crystallinity drops to 54% from 92.6%. We interpret R1120GL as representing the cotectic assemblage of two pyroxenes + plagioclase + magnetite at 1 atm without significant Fe-loss. However, the actual temperature of R1150GL might not have been precisely 1150 °C, given its higher melt fraction compared to R1180GL (Table 2). In this case, any effect of oxidation on the relative stability of magnetite has been countered by the compensatory effects of Fe-loss. In spite of the evident negative effect of Fe-loss on magnetite and ilmenite stability, similarities between our experimental products and those produced by previous studies of similar high-Mg andesite starting materials [e.g. (Grove et al. 2003] suggest that, in most respects, liquidus equilibria in our experiments were not significantly affected by the observed Fe-losses.

Approach to equilibrium during experiments

No attempt was made at reversals during our experiments other than experiments on unfused rock powder. However, several features from our water-saturated experiments on glass starting material suggest that for these experiments equilibrium was sufficiently approached to provide a reliable guide to phase equilibria in the natural high-Mg andesite. These features include: (1) the lack of compositional zoning in crystals and melts as evident from BSE images (Fig. 1); (2) euhedral crystal shapes (Fig. 1); (3) relatively low Fe-loss in most experiments (Table 2); (4) the closeness of mass-balances attained between run products and starting materials for most experiments (with $\sum R^2$ generally < 0.2); and (5) the systematic dependence of element exchange between minerals and melts (e.g. K_d(Fe–Mg) for pyroxene/melt and K_d(Ca–Na) for plagioclase/melt) on run temperatures (Figs. 4 and 5; Table 2; Table SI 5) and their consistency with previously published relationships (Putirka 2008).

For the experiments on unfused rock powder, it is evident that the approach to equilibrium was in most cases either only partial or locally achieved. This is demonstrated by the

predominance of irregular crystal forms and epitaxial growth textures (Fig. 2). The latter are most evident for pyroxenes. We note that K_ds for Fe and Mg exchange between pyroxene rims and melts are the same as for the experiments on glass starting material (Fig. 2b, c, d, f; Table SI4) so that it is likely that local equilibrium was approached. However, the same cannot be said for the crystal cores which produce very low or high K_ds. Considering these facts and the nature of the starting material, it is likely that the pyroxene rims are overgrowths that equilibrated with local melts, whereas the cores are relicts from the original rock (powder). Some olivines and Fe–Ti oxides from the same runs display both euhedral form and compositional homogeneity (Fig. 2d, f) and are also likely to represent equilibrium growth during experiments.

The plagioclase produced during experiments on rock powder and glass exhibits two contrasting forms, as described in the above section. Those from experiments on rock powders are characteristically either, large and irregular, or euhedral and very small. In contrast, plagioclase from experiments on glass starting material tends to be euhedral and large enough to be easily analysed. Calculated K_d(Ca–Na) values for the first group are also either very high or low (1.13–6.22) when compared to results for glass starting material (1.48–2.91) (Fig. 4). Although the crystallites from experiments on unfused rock powder are too small for quantitative analysis, it seems probable that they resulted from coupled dissolution and re-precipitation as the original plagioclase from the rock began to equilibrate with the melt produced during experiments. Therefore, plagioclase was probably a liquidus phase of the co-existing melt. What is noteworthy in the case of the 1 atm experiments is that plagioclase persists to significantly higher temperatures (1220 °C) during experiments on unfused rock powders than it does when the starting material is a glass (1120 °C). In spite of this, the compositions of coexisting melts are only mildly dissimilar for the two starting materials. The main contrast is that, at the same temperatures, melts from experiments on unfused rock powders tend to be slightly more aluminous and silica-rich than is the case for glass starting material.

The pyroxenes produced during water-saturated experiments on glass starting material are mostly homogeneous and have compositions consistent with both run temperatures and natural phenocrysts (Fig. 3). However, for some experiments the Wo concentrations of clinopyroxenes are variable and significantly less than expected for the run temperatures involved. Considering that for most of these cases run temperatures were reduced and the degree of crystallisation comparatively high, it is likely that kinetic factors played a part by inhibiting the unmixing of excess enstatite-ferrosilite. This does not imply that clinopyroxene was not a stable liquidus phase in the experiments concerned.

Liquidus relations and the effects of changing P, T, H_2O and fO_2

When interpreting our results, it is necessary to take into account the predictable effects of Fe-loss in some experiments. These include reductions in the stabilities of magnetite and ilmenite already discussed, together with a reduction in the normative olivine content of the starting composition. The loss of normative olivine will cause a reduction in the stability of olivine relative to both plagioclase and pyroxenes and will also increase the stability of plagioclase relative to pyroxenes. When these effects are allowed for, it is evident that olivine and Cr-spinel are the liquidus phases of glass starting material under water-saturated conditions at pressures of 200 to 500 MPa. Both are removed during progressive crystallisation as orthopyroxene and clinopyroxene become the dominant subliquidus phases. These are followed by plagioclase at 200 MPa whereas at 500 MPa plagioclase is replaced as a subliquidus phase by amphibole. Similar to natural petrographic observations, our experiments suggest co-crystallisation of two pyroxenes and plagioclase likely occurred over an extended temperature interval. This interpretation is supported by: (1) The cotectic relationship observed between these three phases in our 200 MPa experiments; (2) The broad compositional overlap between natural and experimental pyroxenes across a wide temperature range, indicating systematic compositional changes in pyroxene with decreasing temperature. A similar systematic relationship is evident in plagioclase: the K_d (Ca-Na) values for most experimental plagioclase crystallised from glass starting materials fall within the range of natural plagioclase (Figs. 4 and 5). An Fe–Ti oxide is the last phase to crystallise at all pressures and water concentrations. For 200 MPa with fO_2 = NNO + 1 ilmenite is produced. This is replaced by magnetite when fO_2 is increased to NNO + 2. In both the 500 MPa piston- cylinder and 1 atmosphere experiments, magnetite was the stable Fe–Ti oxide.

None of our water-undersaturated experiments duplicated either liquidus or near-liquidus conditions. This factor, combined with significant Fe-loss in some water-undersaturated experiments, leaves it unclear as to whether olivine and Cr-spinel are liquidus phases. Nevertheless, both are absent under subliquidus conditions where both clinopyroxene and orthopyroxene crystallise before plagioclase, although the latter has a significantly larger crystallisation interval than in the water-saturated experiments. At 1 atm orthopyroxene replaces olivine as the liquidus phase. This is joined by plagioclase and clinopyroxene at higher

degrees of crystallisation. Magnetite is a late crystallising phase. The crystallisation interval for plagioclase is notably variable for experiments on glass and unfused starting materials, being larger for the latter than the former.

Because the phase assemblages produced by experiments on unfused whole-rock powders are similar to those from experiments on glass starting materials, with only minor differences (Table 2), the liquidus relations derived from experiments appear to be unaffected by the original state of starting materials. The most relevant features are:

- Olivine and Cr-spinel are either liquidus or potential liquidus phases under high water activities to pressures ≥ 500 MPa, but are replaced by clinopyroxene and orthopyroxene as crystallisation proceeds.
- Plagioclase is a late crystallising phase under hydrous conditions, particularly as pressure and melt-H_2O concentrations increase.
- The early crystallisation of plagioclase together with pyroxenes is induced by low-pressure anhydrous conditions.
- Magnetite and ilmenite are late crystallising phases, particularly for low melt-H_2O concentrations, with the crystallisation of magnetite being favoured by high fO_2.

Conditions of pre-eruptive storage for the 1976–2000 high-Mg andesite magma

Phenocryst modes and matrix glass compositions for the Whakaari high-Mg andesites are most closely replicated by experiments at 1 atm and 200 MPa where melt-water concentrations are low (≤3 wt% H_2O) and the oxygen fugacity around NNO + 1 (Figs. 3, 4, 5 and 6; Fig. SI 7). This confirms results from our previous Rhyolite-MELTS (purple lines) modelling (Jiang et al. 2024), where a best fit to the natural liquid line of descent was achieved at 60 MPa with 0.5 wt% H_2O and fO_2 = NNO + 1 (Fig. 6). Although the suggested H_2O concentrations are very low when compared to those generally expected for arc magmas (e.g. (Plank et al. 2013; Rasmussen et al. 2022; Urann et al. 2022) these low concentrations are confirmed by analyses of H_2O in Whakaari melt inclusions (Esposito et al. 2014; Wardell et al. 2001).

When combined with previously estimated entrapment pressures for melt inclusions (Mandon et al. 2021), our findings suggest that the high-Mg andesite magmas underwent differentiation in a shallow magma chamber (< 200 MPa) and were also relatively dry. The low H_2O-concentrations are unexpected given the usually water-rich nature of most arc magmas (Plank et al. 2013) combined with experimental evidence (Grove et al. 2003; Krawczynski et al. 2012; Tatsumi 1981; Wood and Turner 2009) for the role of water in the production of primary high-Mg andesite magmas. However, it is possible that the magmas were originally more H_2O-rich but became dehydrated owing to degassing following rapid ascent to shallow depths. During this phase olivine was removed either through prior precipitation and/or peritectic reaction following H_2O-loss and progressive crystallisation. Melt evolution then proceeded along the plagioclase + two pyroxene cotectic before olivine was

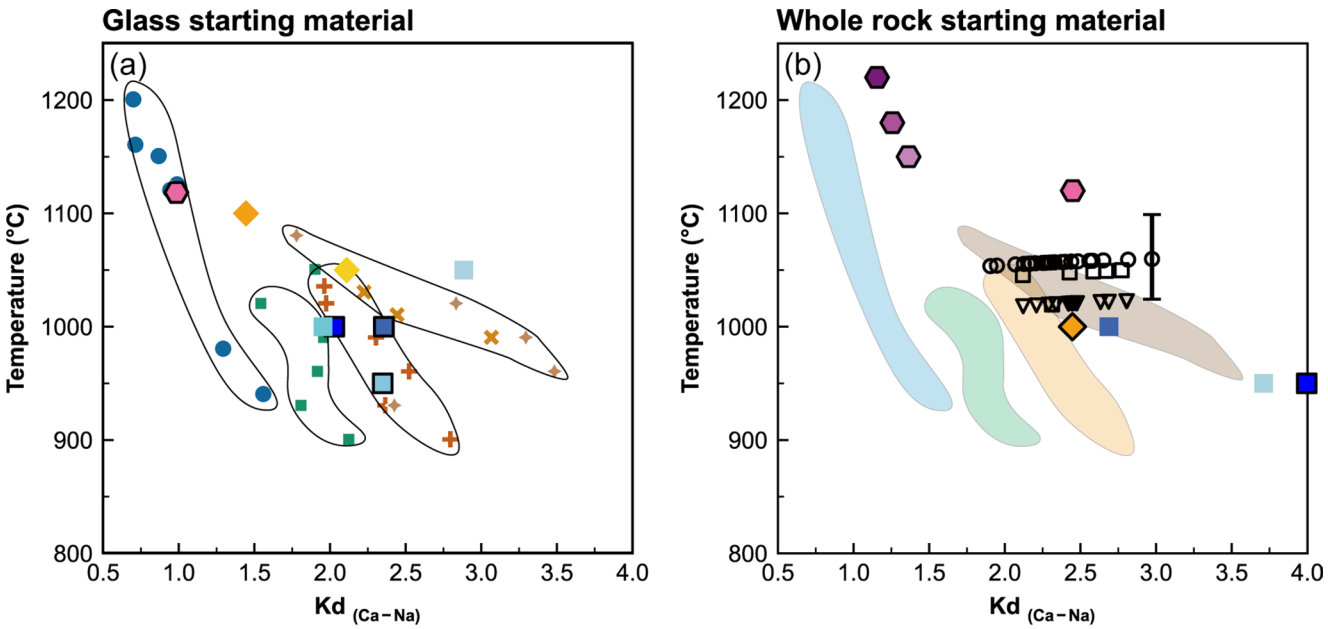

Fig. 5 The relationship between K_d(Ca–Na) ratios of experimental and natural plagioclase and magmatic temperature. The temperatures calculated for natural plagioclase were based on Eq. 23 in Putirka (2008) supposing that the melt water concentration and pressure were 1 wt% and 60 MPa, respectively. The error bar results from the same calculation at 0 wt% and 2 wt% water. The legend can be found in Fig. 4

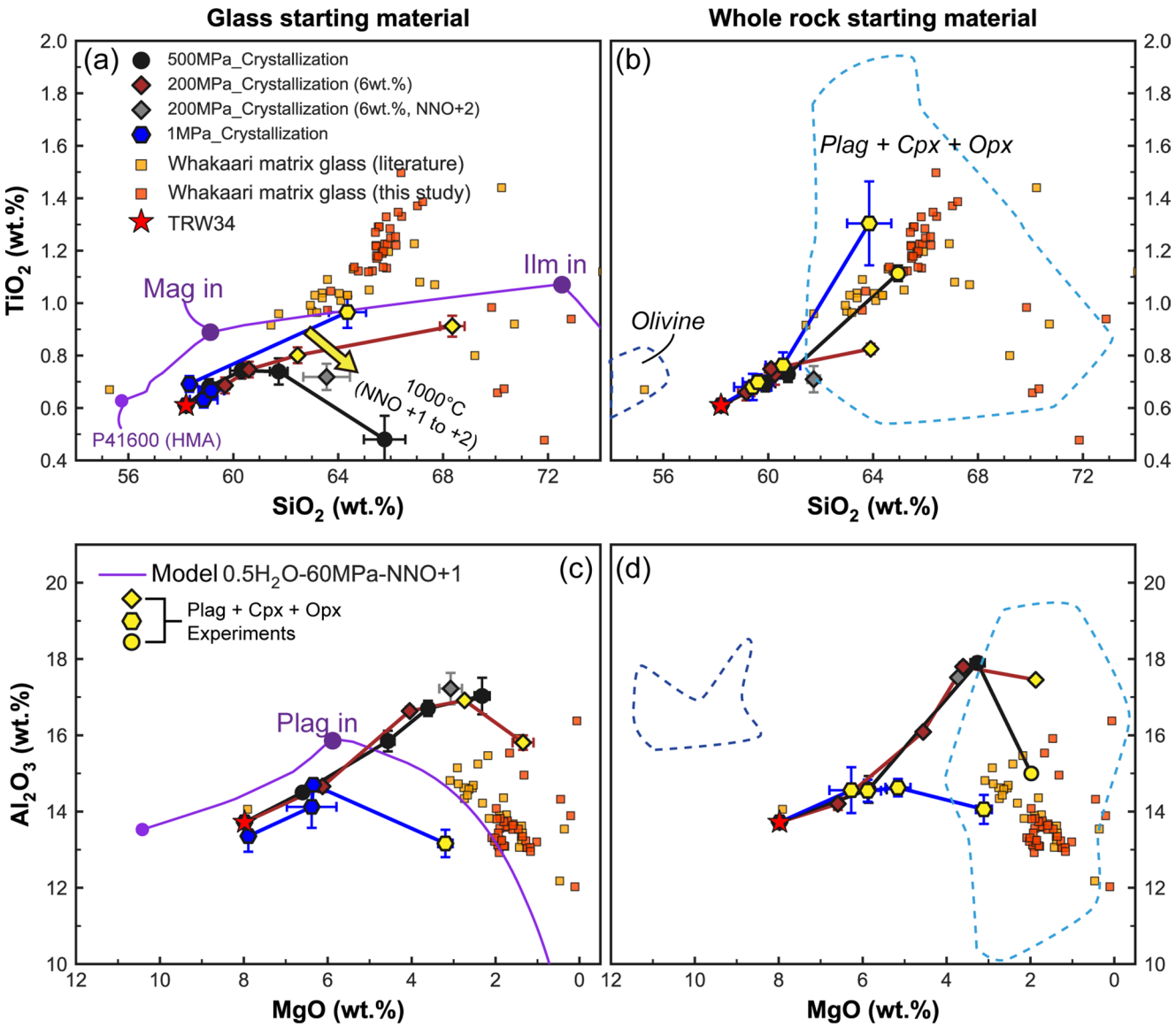

Fig. 6 LLD results of water-saturated and 1 atm experiments using glass staring materials (**a** and **c**) and unfused rock powder materials (**b** and **d**). The temperature denoted next to the scatters represents the end point of different experiments. The solid purple line on the diagram represents the modelling of fractional crystallisation, set at 60 MPa, 2 wt% H_2O, and an oxygen fugacity of NNO + 1, utilizing the Rhyolite-MELTS for simulation. The large, yellow marker symbolize the "appropriate" experiments containing a phase assemblage of plagioclase + clinopyroxene + orthopyroxene. The natural matrix glass compositions and melt inclusions were sourced from previous studies (Heyworth et al. 2007; Kilgour et al. 2021b; Mandon et al. 2021) and this study

re-introduced immediately prior to eruption by mixing with hydrous re-charged magmas.

As previously noted, an outcome of crystallisation under dry conditions would be the early crystallisation of plagioclase (Fig. 7; Fig. SI 8) and late crystallisation of Fe–Ti oxides (Jenner et al. 2010; Sisson and Grove 1993; Zimmer et al. 2010). This provides an explanation for why the natural LLD (as defined by matrix glass compositions) display strong relative Fe/Mg enrichments (Fig. 8c) and only moderate enrichments of Al_2O_3 and TiO_2 when compared to typical calc-alkaline fractionation trends (Fig. 8). It also explains both the absence of amphibole and presence of hercynites in the high-Mg andesites (Fig. SI 9) with the latter being favoured by dry, low-pressure conditions (Woodland and Wood 1990). In view of these factors, evolution of the magmas under lower-crustal conditions is unlikely. Instead, the data are consistent with shallow fractionation which can also be used to explain the development of Whakaari's overlying hydrothermal system, including the crater lake, hot springs, and fumaroles, as a consequence of degassing from underlying magmatic sources (Christenson et al. 2017; Mandon et al. 2021).

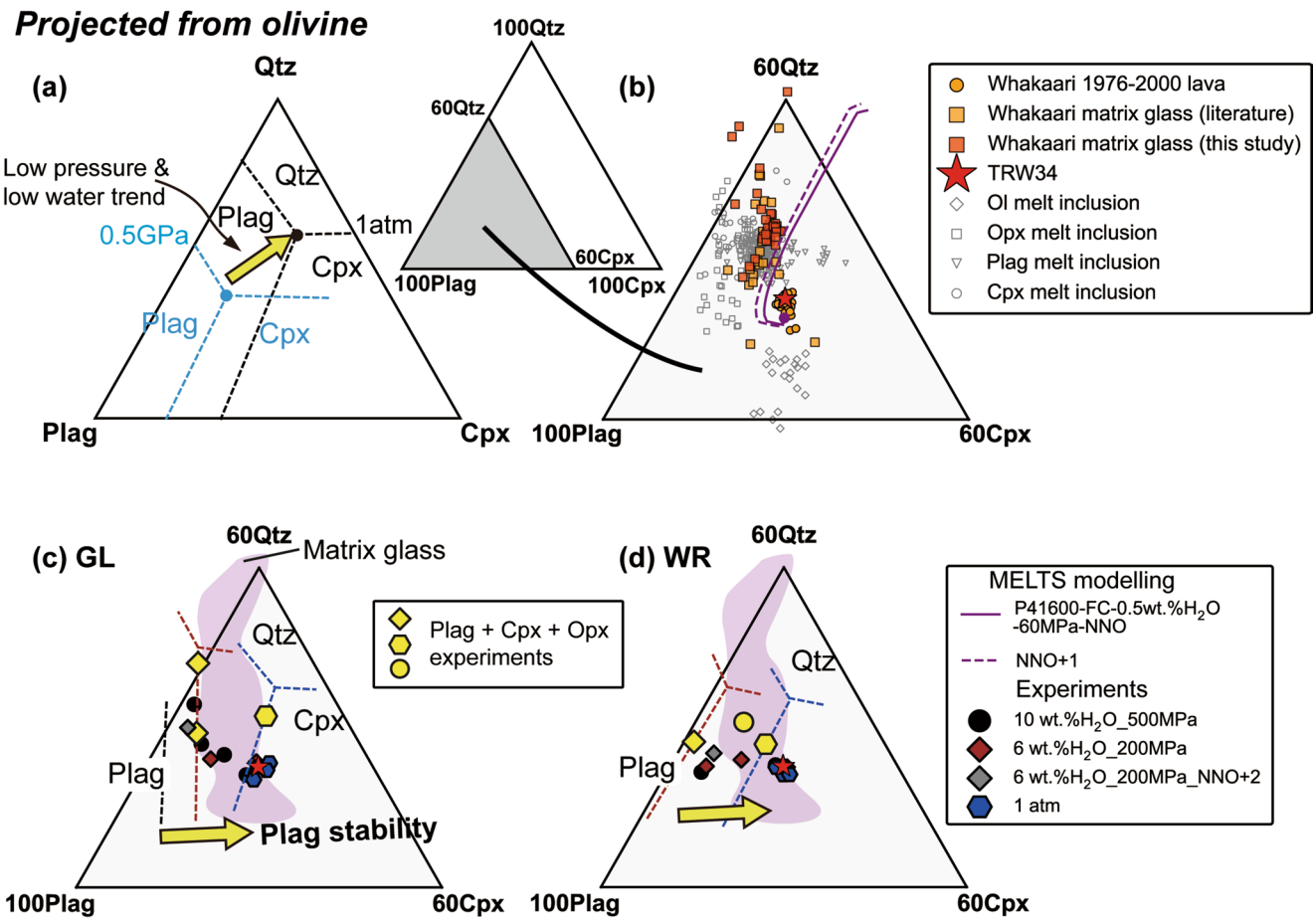

Fig. 7 Compositions of water-saturated glasses and anhydrous glasses on the quartz-plagioclase-clinopyroxene pseudoternary projections from olivine. The transformation of the original oxides to the four apex endmembers was calculated using a methodology outlined by Grove (1993). **a** is a schematic diagram displaying the shift of cotectic relationships as per decreases in water or pressure. **b** shows the distribution of natural melt inclusions (Heyworth et al. 2007; Kilgour et al. 2021b; Mandon et al. 2021), matrix glasses (Mandon et al. 2021), whole rock samples (Cole et al. 2000), and Rhyolite-MELTS simulations. **c** Water-saturated experiments on glass starting materials; **d** Water-saturated experiments on unfused whole rock starting materials. Please note that the cotectic relationships between clinopyroxene and plagioclase (represented by dashed lines) are imprecise estimates in terms of our experimental measurements. However, the shift in the cotectic lines in response to pressure adjustments from 500 MPa to 1 atm is observable

The effects of mixing different generations of phenocrysts and melts

Although the experimental evidence is consistent with magma crystallisation in a shallow reservoir beneath Whakaari, there are aspects of the magmatic system that require further consideration. One is the evident role of magma mixing in the production of high-Mg andesites. This is demonstrated by the co-existence of Fo-rich olivine with evolved matrix glasses in the high-Mg andesites. It is also consistent with the frequency of reversely-zoned overgrowths on pyroxene phenocrysts (Mandon et al. 2021). These relationships are observed even in the most primitive samples and are consistent with mixing between magmas of the same bulk composition, but contrasting degrees of crystallisation. While it was not possible to fully replicate these dynamic processes in our experiments, the consistency of liquidus relations, including melt compositions, for experiments on glass and unfused rock powder suggest that our fundamental conclusions are unlikely to be compromised as a result.

Implications for Arc magma evolution

Conditions of magma differentiation in Arc settings

Shallow magmatic systems have been recognised in volcanic systems worldwide based on a combination of geophysical evidence ((Gudmundsson et al. 1994; Jolly et al. 2017; Nagaoka et al. 2012; Nishi et al. 1996; Patanè et al. 2017; Sturkell et al. 2003) and magmatic phase equilibria (Adam et al. 2016). In spite of this, recent debates on silicic arc magma generation have usually focused on either

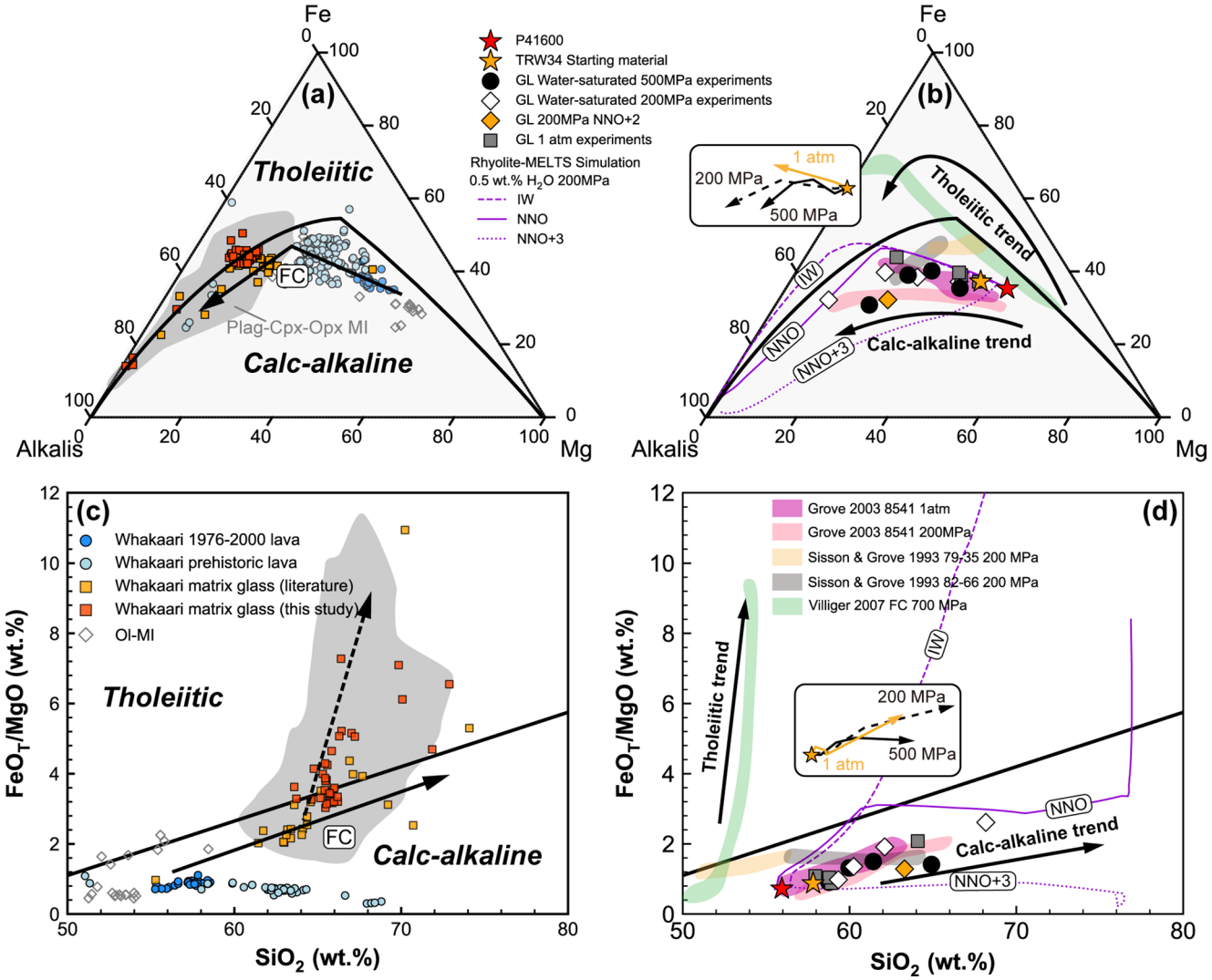

Fig. 8 Calc-alkaline versus tholeiitic trends in Whakaari samples and experimental results. **a** and **b**: AFM diagram; **c** and **d**: SiO_2 (wt%) versus FeO_T/MgO. Discriminant boundaries between calc-alkaline magma and tholeiitic magma in **a** and **b** are from Vermeesch and Pease (2021) and Miyashiro (1974), respectively. The three purple lines illustrate variations in the LLD simulated using Rhyolite-MELTS, modeling magma evolution under conditions of 0.5 wt% initial water content and constant pressure at 200 MPa. The fO_2 value in these simulations ranges from IW (iron-wüstite) to NNO+3. The experimental results are collected from Grove et al. (2003); Sisson and Grove (1993); Villiger et al. (2007). The data source of Whakaari melt inclusions and matrix glasses is reported in Fig. 7. *Ol* livine, *Plag* plagioclase, *Opx* rthopyroxene, *Cpx* clinopyroxene, *MI* melt inclusion, *FC* fractional crystallisation. The three arrow-marked lines in the inset panels of subfigures (b) and (d) depict the LLD trends derived from our experiments under 1 atm, 200 MPa, and 500 MPa conditions (water-saturated)

differentiation at the base of the crust (Annen et al. 2006; Klaver et al. 2018; Solano et al. 2012) or evolution in "trans-crustal magmatic systems" (Cashman et al. 2017; Journeau et al. 2022; Sparks and Cashman 2017; Tattitch et al. 2021). All of these alternatives repeat concerns that were raised during earlier debates over the origins of the calc-alkaline magma series and the reasons for its divergence from the tholeiitic series (Foden and Green 1992; Green and Ringwood 1968; Osborn 1959; Sisson and Grove 1993; Yoder Jr and Tilley 1962).

Our experimental results indicate that, in the particular case of Whakaari, magma evolution under deep-crustal conditions is unlikely. Instead, independently of the affinity of the parent magma, the development of the calc-alkaline trend is shown to be retarded by melt dehydration allowing a weak tholeiitic trend to be developed in its place (Fig. 8a, c). On this basis, our study supports the findings of Osborn (1959) and Sisson and Grove (1993) that highlight the importance of water, rather than deep crustal fractionation, for the evolution of the calc-alkaline trend in arc magmas. Here it is necessary to recall that tholeiitic magmas produced in arc settings can also be water-rich (see Firth et al. (2019). Because of this, other factors related to parent

magma composition, such as the alkali-lime index of Peacock (1931), must also be considered to play a part.

Conclusions

Our experiments indicate that pre-eruptive storage of Whakaari high-Mg andesite magmas occurred at comparatively low pressures (<200 MPa or <6 km), with temperatures >950 °C and fO_2 around ΔNNO+1. These low pressures caused the magmas to undergo significant degassing and consequent crystallisation (30–60%) under comparatively dry conditions (<2 wt% of dissolved H_2O). These conditions favoured the early crystallisation of plagioclase and late appearance of magnetite, driving residual Whakaari melts along a weakly tholeiitic trend. Periodic replenishment by hot and undegassed magmas resulted in the partial re-equilibration of different generations of crystals and melts. These processes added complexity to the petrography of the erupted rocks while also driving overlying hydrothermal activity. Our results highlight the critical role of water, as opposed to deep crustal processes, in the production of calc-alkaline arc magmas.

Supplementary Information The online version contains supplementary material available at https://doi.org/10.1007/s00410-025-02235-3.

Acknowledgements The authors thank Jim W. Cole for providing the samples. We also extend our gratitude to Slava Shcheka, Remi Champallier, and David Clark for their invaluable assistance and guidance with various experimental apparatus. We are also grateful to Andrew Berry for supervising our 1 atm experiments at the Australian National University. We extend our sincere gratitude to the two reviewers, Mike Krawczynski and Peter Ulmer, for their insightful feedback and constructive suggestions, which significantly improve the quality of this manuscript.

Funding Open Access funding enabled and organized by CAUL and its Member Institutions. This research was supported by the New Zealand MIBE Endeavour Grant - Research Programmes: Transitioning Taranaki to a Volcanic Future (No. 3718996). WCJ is supported by a grant from China Scholarship Council (No. 202006410007).

Data availability Most of the data underlying this article are available within the article and its online supplementary material. Additional raw data may be available upon request.

Declarations

Competing Interests We declare no conflicts of interests.

References

Adam J, Locmelis M, Afonso JC, Rushmer T, Fiorentini ML (2014) The capacity of hydrous fluids to transport and fractionate incompatible elements and metals within the earth's mantle. Geochem Geophys Geosyst 15(6):2241–2253. https://doi.org/10.1002/2013gc005199

Adam J, Turner S, Rushmer T (2016) The genesis of silicic Arc magmas in shallow crustal cold zones. Lithos 264:472–494. https://doi.org/10.1016/j.lithos.2016.07.036

Almeev RR, Ariskin AA, Kimura J-I, Barmina GS (2013) The role of polybaric crystallization in genesis of andesitic magmas: phase equilibria simulations of the bezymianny volcanic subseries. J Volcanol Geoth Res 263:182–192. https://doi.org/10.1016/j.jvolgeores.2013.01.004

Andújar J, Martel C, Pichavant M, Samaniego P, Scaillet B, Molina I (2017) Structure of the plumbing system at Tungurahua volcano, ecuador: insights from phase equilibrium experiments on July–August 2006 eruption products. J Petrol 58(7):1249–1278. https://doi.org/10.1093/petrology/egx054

Annen C, Blundy JD, Sparks RSJ (2006) The genesis of intermediate and silicic magmas in deep crustal hot zones. J Petrol 47(3):505–539. https://doi.org/10.1093/petrology/egi084

Barr JA, Grove TL (2010) AuPdFe ternary solution model and applications to Understanding the fO2 of hydrous, high-pressure experiments. Contrib Miner Petrol 160(5):631–643. https://doi.org/10.1007/s00410-010-0497-z

Boyd F, England J (1960) Apparatus for phase-equilibrium measurements at pressures up to 50 Kilobars and temperatures up to 1750° C. J Phys Res 65(2):741–748

Brugier Y-A, Alletti M, Pichavant M (2015) Fe pre-enrichment: a new method to counteract iron loss in experiments on basaltic melts. Am Mineral 100(10):2106–2111

Cashman KV, Edmonds M (2019) Mafic glass compositions: a record of magma storage conditions, mixing and ascent. Philosophical Trans R Soc A 377(2139):20180004

Cashman KV, Giordano G (2014) Calderas and magma reservoirs. J Volcanol Geoth Res 288:28–45. https://doi.org/10.1016/j.jvolgeores.2014.09.007

Cashman KV, Sparks RSJ (2013) How volcanoes work: A 25 year perspective. Geol Soc Am Bull 125(5–6):664–690. https://doi.org/10.1130/b30720.1

Cashman KV, Sparks RS, Blundy JD (2017) Vertically extensive and unstable magmatic systems: a unified view of igneous processes. Science 355(6331). https://doi.org/10.1126/science.aag3055

Chin EJ, Shimizu K, Bybee GM, Erdman ME (2018) On the development of the calc-alkaline and tholeiitic magma series: a deep crustal cumulate perspective. Earth Planet Sci Lett 482:277–287

Christenson BW, White S, Britten K, Scott BJ (2017) Hydrological evolution and chemical structure of a hyper-acidic spring-lake system on whakaari/white island, NZ. J Volcanol Geoth Res 346:180–211. https://doi.org/10.1016/j.jvolgeores.2017.06.017

Clark R, Cole J (1986) White Island. Late Cenozoic Volcanism New Z Royal Soc New Z Bull 23:169–178

Clark R, Otway P (1989) Deformation monitoring associated with the 1976–82 white Island eruption sequence. New Z Geol Surv Bull 103:69–84

Cole J, Graham I (1989) Petrology of strombolian and phreatomagmatic ejecta from the 1976-82 white Island eruption sequence. NZ Geol Surv Bull 103:61–68

Cole J, Thordarson T, Burt R (2000) Magma origin and evolution of white Island (Whakaari) volcano, Bay of plenty, new Zealand. J Petrol 41(6):867–895

Collins S, Pyle D, Maclennan J (2009) Melt inclusions track pre-eruption storage and dehydration of magmas at Etna. Geology 37(6):571–574

Cordell D, Naif S, Troch J, Huber C (2022) Constraining magma reservoir conditions by integrating thermodynamic petrological models and bulk resistivity from magnetotellurics. Geochem Geophys Geosyst 23(9):e2022GC010455

Dempsey DE, Cronin SJ, Mei S, Kempa-Liehr AW (2020) Automatic precursor recognition and real-time forecasting of sudden explosive volcanic eruptions at whakaari, new Zealand. Nat Commun 11(1):3562. https://doi.org/10.1038/s41467-020-17375-2

Droop G (1987) A general equation for estimating Fe3 + concentrations in ferromagnesian silicates and oxides from microprobe analyses, using stoichiometric criteria. Mineral Mag 51(361):431–435

Elsworth D, Mattioli G, Taron J, Voight B, Herd R (2008) Implications of magma transfer between multiple reservoirs on eruption cycling. Science 322(5899):246–248

Erdmann S, Martel C, Pichavant M, Bourdier JL, Champallier R, Komorowski JC, Cholik N (2016) Constraints from phase equilibrium experiments on Pre-eruptive storage conditions in mixed magma systems: a case study on Crystal-rich basaltic andesites from Mount merapi, Indonesia. J Petrol 57(3):535–560. https://doi.org/10.1093/petrology/egw019

Esposito R, Hunter J, Schiffbauer JD, Shimizu N, Bodnar RJ (2014) An assessment of the reliability of melt inclusions as recorders of the pre-eruptive volatile content of magmas. Am Mineral 99(5–6):976–998. https://doi.org/10.2138/am.2014.4574

Firth C, Adam J, Turner S, Rushmer T, Brens R, Green TH, Erdmann S, O'Neill H (2019) Experimental constraints on the differentiation of low-alkali magmas beneath the Tonga Arc: implications for the origin of Arc tholeiites. Lithos 344–345:440–451. https://doi.org/10.1016/j.lithos.2019.07.008

Foden J, Green D (1992) Possible role of amphibole in the origin of andesite: some experimental and natural evidence. Contrib Miner Petrol 109(4):479–493

Gase AC, Van Avendonk HJA, Bangs NL, Luckie TW, Barker DHN, Henrys SA, Bassett D, Okaya DA, Jacobs KM, Kodaira S, Fujie G, Arnulf AF, Yamamoto Y (2019) Seismic evidence of magmatic rifting in the offshore Taupo volcanic zone, new Zealand. Geophys Res Lett 46(22):12949–12957. https://doi.org/10.1029/2019gl085269

Gavrilenko M, Batanova VG, Llovet X, Krasheninnikov S, Koshlyakova AN, Sobolev AV (2023) Secondary fluorescence effect quantification of EPMA analyses of olivine grains embedded in basaltic glass. Chem Geol 621. https://doi.org/10.1016/j.chemgeo.2023.121328

Ghiorso MS, Gualda GA (2015) An H2O–CO2 mixed fluid saturation model compatible with rhyolite-MELTS. Contrib Miner Petrol 169(6):1–30

Giordano G, Caricchi L (2022) Determining the state of activity of transcrustal magmatic systems and their volcanoes. Annu Rev Earth Planet Sci 50:231–259

Green DH (1976) Experimental testing of equilibrium partial melting of peridotite under water-saturated, high-pressure conditions. Can Mineral 14(3):255–268

Green TH, Ringwood A (1968) Origin of Garnet phenocrysts in calc-alkaline rocks. Contrib Miner Petrol 18(2):163–174

Green TH, Ringwood A, Major A (1966) Friction effects and pressure calibration in a piston-cylinder apparatus at high pressure and temperature. J Phys Res 71(14):3589–3594

Grove TL (1993) Corrections to expressions for calculating mineral components in origin of calc-alkaline series lavas at medicine lake volcano by fractionation, assimilation and mixing and experimental petrology of normal MORB near the Kane fracture zone: 22°-25° N, mid-atlantic ridge. Contrib Miner Petrol 114(3):422–424

Grove TL, Elkins-Tanton LT, Parman SW, Chatterjee N, Müntener O, Gaetani GA (2003) Fractional crystallization and mantle-melting controls on calc-alkaline differentiation trends. Contrib Miner Petrol 145(5):515–533. https://doi.org/10.1007/s00410-003-0448-z

Gualda GAR, Ghiorso MS, Lemons RV, Carley TL (2012) Rhyolite-MELTS: a modified calibration of MELTS optimized for Silica-rich, Fluid-bearing magmatic systems. J Petrol 53(5):875–890. https://doi.org/10.1093/petrology/egr080

Gudmundsson O, Brandsdóttir B, Menke W, Sigvaldason G (1994) The crustal magma chamber of the Katla volcano in South Iceland revealed by 2-D seismic undershooting. Geophys J Int 119(1):277–296

Hammer JE, Rutherford MJ, Hildreth W (2002) Magma storage prior to the 1912 eruption at novarupta, Alaska. Contrib Miner Petrol 144:144–162

Heyworth Z, Turner S, Schaefer B, Wood B, George R, Berlo K, Cunningham H, Price R, Cook C, Gamble J (2007) 238U–230Th–226Ra–210Pb constraints on the genesis of high-Mg andesites at white island, new Zealand. Chem Geol 243(1–2):105–121. https://doi.org/10.1016/j.chemgeo.2007.05.012

Hughes EC, Biasi J, Fendley I, Rahilly K, Schlieder TD, Winslow H, Fischer TP, Wallace PJ (2024) Modeling the behavior of sulfur in magmatic systems from source to surface: application to whakaari/white island, Aotearoa new zealand, and etna, Italy. J Volcanol Geoth Res 446:107939

Iacovino K, Guild MR, Till CB (2020) Aqueous fluids are effective oxidizing agents of the mantle in subduction zones. Contrib Miner Petrol 175(4):36. https://doi.org/10.1007/s00410-020-1673-4

Jakobsson S (2012) Oxygen fugacity control in piston-cylinder experiments. Contrib Miner Petrol 164(3):397–406. https://doi.org/10.1007/s00410-012-0743-7

Jenner FE, O'Neill HSTC, Arculus RJ, Mavrogenes JA (2010) The magnetite crisis in the evolution of Arc-related magmas and the initial concentration of au, ag and Cu. J Petrol 51(12):2445–2464. https://doi.org/10.1093/petrology/egq063

Jiang W-C, Adam J, Firth C, Turner S, Rushmer T, Cronin S (2024) Magma evolution and storage conditions in an Andesite–Dacite volcanic system, Whakaari (White Island), New Zealand. J Petrol 65(9):egae091

Jolly AD, Lokmer I, Thun J, Salichon J, Fry B, Chardot L (2017) Insights into fluid transport mechanisms at white Island from analysis of coupled very long-period (VLP), long-period (LP) and high-frequency (HF) earthquakes. J Volcanol Geoth Res 343:75–94. https://doi.org/10.1016/j.jvolgeores.2017.06.006

Jorgenson C, Higgins O, Petrelli M, Begue F, Caricchi L (2022) A machine Learning-Based approach to clinopyroxene thermobarometry: model optimization and distribution for use in Earth sciences. J Geophys Res Solid Earth 127(4). e2021JB022904

Journeau C, Shapiro NM, Seydoux L, Soubestre J, Koulakov IY, Jakovlev AV, Abkadyrov I, Gordeev EI, Chebrov DV, Droznin DV (2022) Seismic tremor reveals active trans-crustal magmatic system beneath Kamchatka volcanoes. Sci Adv 8(5):eabj1571

Kägi R, Müntener O, Ulmer P, Ottolini L (2005) Piston-cylinder experiments on H2O undersaturated Fe-bearing systems: an

experimental setup approaching f O2 conditions of natural calc-alkaline magmas. Am Mineral 90(4):708–717
Kilgour G, Kennedy B, Scott B, Christenson B, Jolly A, Asher C, Rosenberg M, Saunders K (2021a) Whakaari/White island: a review of new zealand's most active volcano. NZ J Geol Geophys 64(2–3):273–295. https://doi.org/10.1080/00288306.2021.1918186
Kilgour G, Moune S, Christenson B, Pasqua FD (2021b) Insights into the 1976–2000 eruption episode of whakaari/white island, new zealand: an eruption fuelled by repeated mafic recharge. Bull Volcanol 83(6). https://doi.org/10.1007/s00445-021-01460-5
Klaver M, Blundy JD, Vroon PZ (2018) Generation of Arc rhyodacites through cumulate-melt reactions in a deep crustal hot zone: evidence from Nisyros volcano. Earth Planet Sci Lett 497:169–180
Krawczynski MJ, Grove TL, Behrens H (2012) Amphibole stability in primitive Arc magmas: effects of temperature, H2O content, and oxygen fugacity. Contrib Miner Petrol 164(2):317–339. https://doi.org/10.1007/s00410-012-0740-x
Kress VC, Carmichael IS (1991) The compressibility of silicate liquids containing Fe 2 O 3 and the effect of composition, temperature, oxygen fugacity and pressure on their redox States. Contrib Miner Petrol 108:82–92
Lindsley DH, Andersen DJ (1983) A two-pyroxene thermometer. J Geophys Re 88(S02):A887–A906
Magee C, Stevenson CT, Ebmeier SK, Keir D, Hammond JO, Gottsmann JH, Whaler KA, Schofield N, Jackson CA, Petronis MS (2018) Magma plumbing systems: a geophysical perspective. J Petrol 59(6):1217–1251
Mandon CL, Christenson BW, Seward TM, Schipper CI (2021) Magma mixing, degassing and late sulfide saturation: insights into the 1976–2000 eruptive sequence at white island, new Zealand. J Volcanol Geoth Res 417. https://doi.org/10.1016/j.jvolgeores.2021.107299
Marxer F, Ulmer P, Müntener O (2023) Ascent-driven differentiation: a mechanism to keep Arc magmas metaluminous? Contrib Miner Petrol 178(8). https://doi.org/10.1007/s00410-023-02035-7
Matjuschkin V, Brooker RA, Tattitch B, Blundy JD, Stamper CC (2015) Control and monitoring of oxygen fugacity in piston cylinder experiments. Contrib Miner Petrol 169(1). https://doi.org/10.1007/s00410-015-1105-z
Melekhova E, Blundy J, Robertson R, Humphreys MCS (2015) Experimental evidence for polybaric differentiation of primitive Arc basalt beneath st. Vincent, lesser Antilles. J Petrol 56(1):161–192. https://doi.org/10.1093/petrology/egu074
Melekhova E, Blundy J, Martin R, Arculus R, Pichavant M (2017) Petrological and experimental evidence for differentiation of water-rich magmas beneath st. Kitts, lesser Antilles. Contrib Miner Petrol 172(11):98. https://doi.org/10.1007/s00410-017-1416-3
Miyashiro A (1974) Volcanic rock series in Island arcs and active continental margins. Am J Sci 274(4):321–355
Nagaoka Y, Nishida K, Aoki Y, Takeo M, Ohminato T (2012) Seismic imaging of magma chamber beneath an active volcano. Earth Planet Sci Lett 333–334:1–8. https://doi.org/10.1016/j.epsl.2012.03.034
Neave DA, Putirka KD (2017) A new clinopyroxene-liquid barometer, and implications for magma storage pressures under Icelandic rift zones. Am Mineral 102(4):777–794. https://doi.org/10.2138/am-2017-5968
Nishi Y, Sherburn S, Scott BJ, Sugihara M (1996) High-frequency earthquakes at white Island volcano, new zealand: insights into the shallow structure of a volcano-hydrothermal system. J Volcanol Geoth Res 72(3–4):183–197
Osborn EF (1959) Role of oxygen pressure in the crystallization and differentiation of basaltic magma. Am J Sci 257(9):609–647
Papale P, Moretti R, Barbato D (2006) The compositional dependence of the saturation surface of H2O+CO2 fluids in silicate melts. Chem Geol 229(1–3):78–95. https://doi.org/10.1016/j.chemgeo.2006.01.013
Patanè D, Barberi G, De Gori P, Cocina O, Zuccarello L, Garcia-Yeguas A, Castellano M, D'Alessandro A, Sgroi T (2017) The shallow magma chamber of Stromboli volcano (Italy). Geophys Res Lett 44(13):6589–6596. https://doi.org/10.1002/2017gl073008
Peacock MA (1931) Classification of igneous rock series. J Geol 39(1):54–67
Peltier A, Scott B, Hurst T (2009) Ground deformation patterns at white Island volcano (New Zealand) between 1967 and 2008 deduced from levelling data. J Volcanol Geoth Res 181(3–4):207–218. https://doi.org/10.1016/j.jvolgeores.2009.01.020
Petrelli M, Caricchi L, Perugini D (2020) Machine learning thermobarometry: application to clinopyroxene-bearing magmas. J Geophys Res 125(9):e2020JB020130
Phillips M, Till CB (2021) Crustal storage and ascent history of the mt. Shasta primitive Magnesian andesite: implications for Arc magma crustal flux rates. Contrib Miner Petrol 177(1). https://doi.org/10.1007/s00410-021-01853-x
Plank T, Kelley KA, Zimmer MM, Hauri EH, Wallace PJ (2013) Why do mafic Arc magmas contain ~4wt% water on average? Earth Planet Sci Lett 364:168–179. https://doi.org/10.1016/j.epsl.2012.11.044
Popa R-G, Bachmann O, Huber C (2021) Explosive or effusive style of volcanic eruption determined by magma storage conditions. Nat Geosci 14(10):781–786. https://doi.org/10.1038/s41561-021-00827-9
Prissel K, Olive JA, Krawczynski MJ (2023) A log-ratio-based algorithm for petrologic mass-balance problems and uncertainty assessment. Geochem Geophys Geosyst 24(12):e2023GC011234
Putirka KD (2005) Igneous thermometers and barometers based on plagioclase+liquid equilibria: tests of some existing models and new calibrations. Am Mineral 90(2–3):336–346
Putirka KD (2008) Thermometers and barometers for volcanic systems. Rev Mineral Geochem 69(1):61–120. https://doi.org/10.2138/rmg.2008.69.3
Rapien M, Bodnar R, Simmons S, Szabo C, Wood C, Sutton S (2003) Melt inclusion study of the embryonic porphyry copper system at white island, new Zealand. Spec Publ-Soc Econ Geol 10:41–60
Rasmussen DJ, Plank TA, Roman DC, Zimmer MM (2022) Magmatic water content controls the pre-eruptive depth of Arc magmas. Science 375(6585):1169–1172
Scaillet B, Pichavant M, Cioni R (2008) Upward migration of vesuvius magma chamber over the past 20,000 years. Nature 455(7210):216–219
Severs MJ, Beard JS, Fedele L, Hanchar JM, Mutchler SR, Bodnar RJ (2009) Partitioning behavior of trace elements between dacitic melt and plagioclase, orthopyroxene, and clinopyroxene based on laser ablation ICPMS analysis of silicate melt inclusions. Geochim Cosmochim Acta 73(7):2123–2141. https://doi.org/10.1016/j.gca.2009.01.009
Shiraki K, Saito T, Kuroda N, Urano H, Sugiura T, Cole J (1994) Magnesian andesites from white island, new zealand: mineralogical evidence for mixing of high-magnesian basalt and dacite magmas. Geosci Rep Shizuoka Univ 20:33–40
Sisson T, Grove T (1993) Experimental investigations of the role of H 2 O in calc-alkaline differentiation and subduction zone magmatism. Contrib Miner Petrol 113:143–166
Solano J, Jackson M, Sparks R, Blundy JD, Annen C (2012) Melt segregation in deep crustal hot zones: a mechanism for chemical differentiation, crustal assimilation and the formation of evolved magmas. J Petrol 53(10):1999–2026
Sparks RSJ, Cashman KV (2017) Dynamic magma systems: implications for forecasting volcanic activity. Elements 13(1):35–40. https://doi.org/10.2113/gselements.13.1.35

Spinks KD, Acocella V, Cole JW, Bassett KN (2005) Structural control of volcanism and caldera development in the transtensional Taupo volcanic zone, new Zealand. J Volcanol Geoth Res 144(1–4):7–22. https://doi.org/10.1016/j.jvolgeores.2004.11.014

Sturkell E, Sigmundsson F, Einarsson P (2003) Recent unrest and magma movements at Eyjafjallajökull and Katla volcanoes, Iceland. J Geophys Res 108(B8)

Tatsumi Y (1981) Melting experiments on a high-magnesian andesite. Earth Planet Sci Lett 54(2):357–365

Tattitch B, Chelle-Michou C, Blundy J, Loucks RR (2021) Chemical feedbacks during magma degassing control Chlorine partitioning and metal extraction in volcanic arcs. Nat Commun 12(1):1774. https://doi.org/10.1038/s41467-021-21887-w

Urann BM, Le Roux V, Jagoutz O, Müntener O, Behn MD, Chin EJ (2022) High water content of Arc magmas recorded in cumulates from subduction zone lower crust. Nat Geosci 15(6):501–508. https://doi.org/10.1038/s41561-022-00947-w

Vermeesch P, Pease V (2021) A genetic classification of the tholeiitic and calc-alkaline magma series. Geochemical Perspect Lett 19:1–6

Villiger S, Ulmer P, Müntener O (2007) Equilibrium and fractional crystallization experiments at 0· 7 gpa; the effect of pressure on phase relations and liquid compositions of tholeiitic magmas. J Petrol 48(1):159–184

Wardell LJ, Kyle PR, Dunbar N, Christenson B (2001) White Island volcano, new zealand: carbon dioxide and sulfur dioxide emission rates and melt inclusion studies. Chem Geol 177(1–2):187–200

Waters LE, Lange RA (2015) An updated calibration of the plagioclase-liquid hygrometer-thermometer applicable to basalts through rhyolites. Am Mineral 100(10):2172–2184

Wieser PE, Kent AJ, Till CB (2023a) Barometers behaving badly II: A critical evaluation of Cpx-only and Cpx-Liq thermobarometry in variably-hydrous Arc magmas. J Petrol:egad050

Wieser PE, Kent AJ, Till CB, Donovan J, Neave DA, Blatter DL, Krawczynski MJ (2023b) Barometers behaving badly I: assessing the influence of analytical and experimental uncertainty on clinopyroxene thermobarometry calculations at crustal conditions. J Petrol 64(2):egac126

Wilson CJN, Rowland JV (2016) The volcanic, magmatic and tectonic setting of the Taupo volcanic zone, new zealand, reviewed from a geothermal perspective. Geothermics 59:168–187. https://doi.org/10.1016/j.geothermics.2015.06.013

Wood BJ, Turner SP (2009) Origin of primitive high-Mg andesite: constraints from natural examples and experiments. Earth Planet Sci Lett 283(1–4):59–66. https://doi.org/10.1016/j.epsl.2009.03.032

Woodland AB, Wood BJ (1990) The breakdown of hercynite at low fO2. Am Mineral 75(11–12):1342–1348

Yoder H Jr, Tilley CE (1962) Origin of basalt magmas: an experimental study of natural and synthetic rock systems. J Petrol 3(3):342–532

Zimmer MM, Plank T, Hauri EH, Yogodzinski GM, Stelling P, Larsen J, Singer B, Jicha B, Mandeville C, Nye CJ (2010) The role of water in generating the calc-alkaline trend: new volatile data for Aleutian magmas and a new tholeiitic index. J Petrol 51(12):2411–2444